Behaviour of a novel timber-concrete floor with a three-dimensional (3D) ductile notched connection

Adham Al Rahim, Piseth Heng, Pisey Keo, Clemence Lepourry-Nicollet, Franck Palas, Hugues Somja

Behaviour of a novel timber-concrete floor with a three-dimensional (3D) ductile notched connection

Adham Al Rahim[a], Piseth Heng[a,*], Pisey KEO[a,*], Clemence Lepourry-Nicollet[a,b], Franck Palas[c], Hugues Somja[a]

[a] *INSA de Rennes, LGCGM/Structural Engineering Research Group, 20, avenue des Buttes de Coësmes, CS 70839, F-35708 Rennes Cedex 7, France*

[b] *INGENOVA, Civil Engineering Office, 5 Rue Louis Jacques Daguerre, 35136 Saint-Jacques-de-la-Lande, France*

[c] *Concept Technique Design R & D, 89 Boulevard de laval, 35500 Vitré, France*

*Corresponding authors: h.piseth168@gmail.com/ pisey.keo@insa-rennes.fr

Abstract

As the sustainability is becoming a new trend in construction, there is a growing inclination towards utilizing timber-concrete composite structures. This paper introduces a system of timber-concrete composite (TCC) floor with three-dimensional (3D) ductile notched connectors. In this system, the web of the timber beam is embedded into the concrete drops so that the notched timber-concrete interface is made of three shear planes instead of one as typically observed in conventional notched connections. This aims to enhance the concrete shear resistance and to prioritize the timber compressive failure, thus achieving a ductile behaviour of the notched connectors. The trapezoidal shape of the connection creates a geometrical interlocking between the timber and the concrete layers for uplift resistance, so that supplementary mechanical steel elements are not necessary. Three symmetrical push-out tests of the proposed notched connectors have been conducted. The results show that the connectors have a remarkable stiffness, strength, and ductility with the failure mode primarily governed by local timber crushing. In addition, three inversed six-point bending tests are performed on TCC floor specimens with a span of 6.55 m. As the self-weight of the specimen and the loading device is non-negligible, this novel test setup is particularly designed to be able to measure deformations and deflections, as well as initial stiffness at a lower load level. The failure mode for all specimens is governed by tensile rupture of the timber beam. The results also show that the proposed connection is effective in limiting slips and uplifts along the beam span. At last, the γ-method is adopted in order to estimate the bending stiffness of the TCC floor with an adaptation to take into account the concrete cracking phenomenon. The comparison with experimental results shows that the adapted γ-method provides a conservative estimation of the bending stiffness with reasonable margin of error at both serviceability and ultimate limit states.

Keywords: Timber-concrete composite slabs, 3D ductile notched connection, Push-Out test, Inversed six-point bending test, γ-method.

1. Introduction

In the last few decades, with the rapid growth of the worldwide population, the building sector contributes up to 30% of global annual greenhouse gas emissions and consumes up to 40% of all energy [1]. Therefore, in France, new environmental regulations, such as RE2020, stimulate the interest of using sustainable and eco-friendly materials in the construction sector. With notable environmental benefits of timber [2], [3], [4], in addition to its interesting mechanical characteristics [5], engineered timber experiences a rapid expansion in its utilization within the construction industry. Nevertheless, the implementation of timber structures can be constrained due to the limitation of deflections imposed for flexural members. To mitigate this problem, the timber-concrete composite (TCC) members have been proposed by incorporating a concrete slab on the top of the timber beam/floor using shear connections. Combining the advantages of both materials, TCC slabs present further advantages in comparison to timber floors [6]. These advantages comprise enhanced strength and stiffness [7], acoustic isolation [8]-[9], dynamic performance [10], and fire resistance [11].

At the interface between timber and concrete, the shear connectors play an important role in transferring longitudinal shear forces. In pursuit of achieving optimal composite action and longer span, various types of shear connections have been proposed and extensively investigated in the literature. The commonly used connections are dowel-type fasteners (e.g. steel screws [12]-[13], steel dowels [15]-[16], steel nails [17]-[18], etc.), notches with and without steel elements [20]-[21] and glued connections [22]-[23].

Dowel-type fasteners are one of the methods used with timber-concrete composite deck in new structures, as well as in historic building renovations for strengthening and stiffening wooden floors. Nevertheless, the TCC floor systems using this type of connections have a limited degree of composite action due to their low shear stiffness and resistance [7]. The use of inclined screws joints with a forward angle of 45° can enhance the shear stiffness of the connection compared to the vertical ones [13]-[14]. However, the installation of dowel-type fasteners is time consuming.

Glued connections, including pure bonded and glued-in shear connectors, are recognized for their high shear strength and ability to achieve high level of composite action. For instance, in bending tests, glued-in steel mesh plates, known as HBV joints, achieved 99% composite action, as demonstrated by Bathon et al. [24]. However, some drawbacks of TCC systems employing an adhesive connection are the vulnerability to brittle failure modes and the low ductility [25], [26], [27].

Another viable method for connecting timber and concrete is thus by cutting grooves in the timber and subsequently filling them with concrete, referred to as notched connection. Notches are commonly regarded as one of the most efficient and cost-effective methods of connection [20]. In such a configuration, the shear forces are transmitted by the contact pressure of the timber on the concrete or vice versa at the notches. Therefore, the mechanical behaviour and failure mechanisms are influenced by both the geometry of the groove and the mechanical properties of timber and concrete. It was demonstrated in [28] that the shear capacity and the stiffness of rectangular notch connectors were proportional to the groove dimensions. Additionally, it has been shown that triangular groove connections exhibited superior performance compared to rectangular ones [29].

According to a recent literature review [30], one of the most common failures observed in notch connectors is the brittle concrete shear failure. Moreover, usual rectangular notches are not able to provide a satisfying uplift

resistance. For this reason, mechanical fasteners, such as coach screws, are used to enhance the uplift resistance and the post-peak behaviour as well as to achieve ductile failures [31]. However, the installation of these steel fasteners increases the construction time and cost. Ouch et al. [32] proposed a dovetail-shaped notched connector for CLT-concrete composite slabs. This shape of the connection is chosen in order to provide an uplift resistance without the use of mechanical fasteners. However, the studied connection shows a low ductility as the failure mode is governed by the shear failure of the cross layer of the CLT.

In notch connections, four different failure modes can occur [47]: longitudinal shear in timber, compression parallel to grain in timber, shear in concrete, and compression in concrete. To be able to obtain a ductile behaviour, two of them (i.e. compression parallel to grain in timber and shear in concrete) as suggested by the technical report COST [47] should be prioritized.

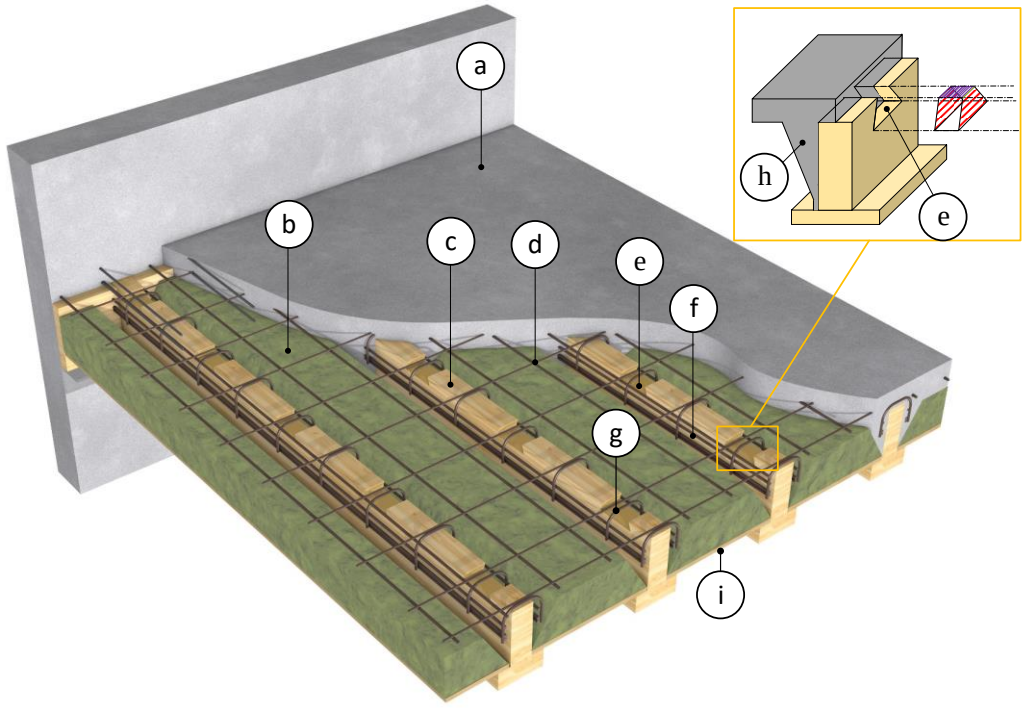

Figure 1: Three-dimensional view of timber-concrete composite floor: (a) concrete slab, (b) bio-based insulation material, (c) inverted T-shaped timber beam, (d) steel mesh, (e) trapezoidal groove, (f) longitudinal steel rebars, (g) transverse U steel rebars, (h) concrete drops, (i) Oriented Strand Board.

In this paper, a novel TCC floor system is proposed (Figure 1). The system comprises inverted T-shaped timber beams embedded into the concrete slab. The flange of the timber beam serves as a support for bio-based isolation blocks and their Oriented Strand Board panel cover. The latter is resistant enough to support the weight of the concrete during casting. The geometry of the insulation blocks creates concrete drops that cover the web of the timber beam. Overall, the system ensures an aesthetic timber aspect of the bottom face of the floor, a good energetic and environmental performance, and an easy casting of the concrete. The timber-concrete connection is ensured by notches on the upper face of the timber beam. At the timber-concrete connection interface, there are three shear planes across the top, left and right surfaces of the groove, thanks to the reinforced concrete drops. The former is used to confine the timber within the notch, thereby improving the ductility of the timber in compression. The latter serves to enhance the resistance of the floor in normal conditions as well as in fire situations. Moreover, the

notched connectors are designed with a trapezoidal shape to prevent the uplift between the two components without the need of mechanical fasteners.

This paper is organized into two main parts. The first one focuses on the experimental investigations on the behaviour of the proposed TCC system. Firstly, three symmetrical push-out tests are conducted in order to have an insight into the behaviour of the proposed notch connectors. In addition, a comparative study of the proposed notched connectors with the ones available in the literature is performed. Next, three full-scale timber-concrete floors with proposed notch connectors are tested under inversed 6-point bending tests. As the self-weight of the specimen and the loading device is non-negligible, this novel test setup is particularly designed to be able to measure deformations and deflections, as well as initial stiffness at a lower load level. Furthermore, several cycles have been applied to the specimen to investigate their impact on the flexural stiffness. The bending stiffness and resistance, the interfacial slips and uplifts along the beam length, as well as failure patterns of the floors are then determined. Besides, in order to evaluate the actual resistance and the modulus of elasticity of timber along with their respective coefficients of variation, several tests have been conducted. Nine timber samples are tested in compression for the timber used in the push-out tests, while another ten samples in compression, ten in tension, and ten in bending for the timber used in the timber-concrete floor flexural tests. The second main part of the paper presents the analytical investigation on the behaviour of the proposed TCC system using the γ-method as presented in Eurocode 5 [35]. It is worth mentioning that this method is adapted to the configuration of the present TCC floor system and to take into account the phenomenon of concrete cracking. The adapted γ-method is validated by comparing its results against the experimental ones.

2. Experimental program

2.1 Symmetrical push-out tests

The purpose of this experimental study is to evaluate the strength, stiffness, ductility, and failure of the notched connection system by conducting a set of three symmetrical push-out tests, noted by S_1, S_2, and S_3.

2.1.1 Description of test specimens

A set of three identical specimens was manufactured and tested in symmetrical push-out configuration at the Laboratory LGCGM of INSA Rennes. Push-out specimens were pre-designed and fabricated in accordance to the geometrical configuration illustrated in Figure 2 by adopting the guidelines provided in the BNTEC TS 19103 [40] for the classical notched connections with standard geometry. Each test specimen consists of two glued timber panels connected to two concrete slabs by means of two notched connectors per side (see Figure 2(a)). The glued timber panel has a dimension of 70 × 360 × 1020 mm and the spacing of the notched connectors is 326 mm (see Figure 2(b)). The overall dimensions of the concrete slabs are 80 × 450 × 1120 mm. The length, width, and depth of the trapezoidal groove in the timber panels are 116 × 70 × 28 mm, respectively (see Figure 2(c) and Figure 2(d)). With the concrete drops, the notched connectors have three shear planes. Timber panels are embedded into the concrete slabs with a vertical offset of 100 mm at the upper part of the specimen. It is worth mentioning that

the folds in concrete drops do not have any function; they are solely a result of the fabrication of the concrete formwork for the specimens (see Figure 2(d)).

Before concrete casting, the two timber panels were glued together as shown in Figure 2(e). They were also painted to reduce friction and to ensure a smooth contact between the materials. The concrete slabs were reinforced with a welded steel mesh with 6 mm diameter spaced at 200 mm in both directions. In turn, the notched connectors were reinforced with transversal U-shaped rebars with a diameter of 6 mm spaced at 426 mm in longitudinal direction. The concrete drops were reinforced with transversal U-shaped rebars with 6 mm diameter. They were connected together by means of two longitudinal rebars per side (see Figure 2(f) and Figure A. 1). The transversal and longitudinal rebars had the same diameter. For all specimens, the first of the two concrete slabs, referred to as slab 1, was cast in a horizontal position. After two days, the specimens were lifted and turned over for casting the second slab, referred to as slab 2.

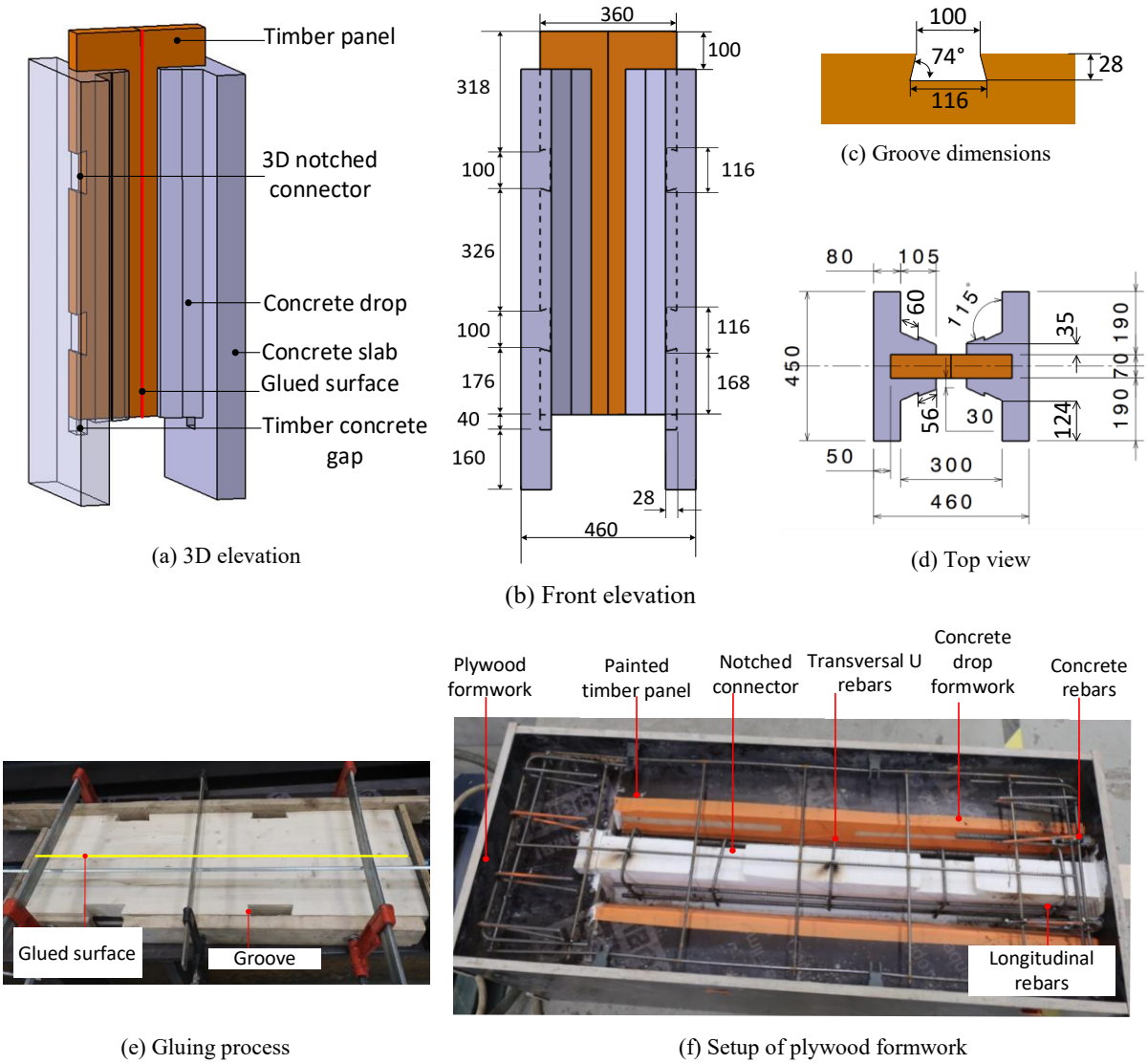

(a) 3D elevation

(b) Front elevation

(c) Groove dimensions

(d) Top view

(e) Gluing process

(f) Setup of plywood formwork

Figure 2: Geometry and fabrication of push-out specimens (dimensions in mm).

2.1.2 Test setup and loading procedure

Illustrated in Figure 3, the testing device was composed of a 1000 kN hydraulic jack with a stroke length of 200 mm, a loading steel plate, and a supporting system (see Figure 3(a) and Figure 3(b)). Eight slip LVDTs with a stroke length of 25 mm and eight uplift LVDTs with stroke lengths of 2.5 mm and 6 mm were positioned on the two sides of the specimen (Figure 3(c)).

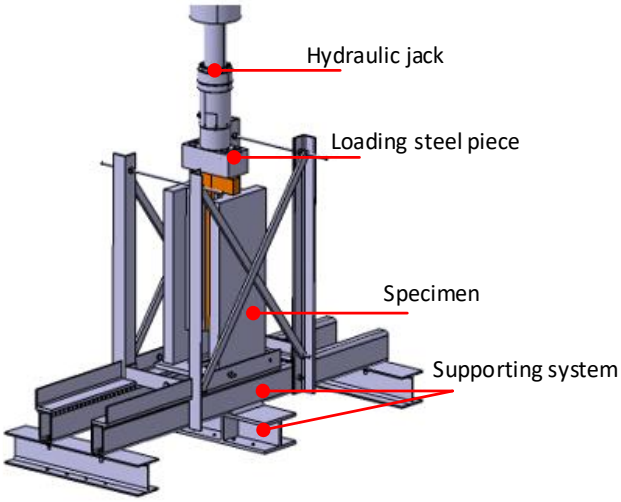

(a) 3D view of the testing device

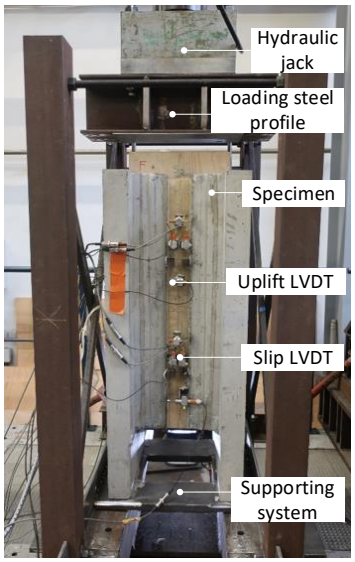

(b) Photograph of the testing device

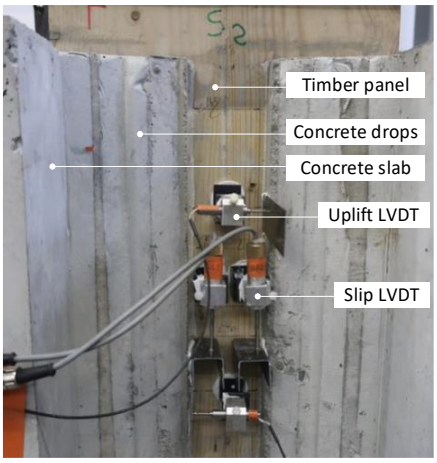

(c) Zoom on LVDTs

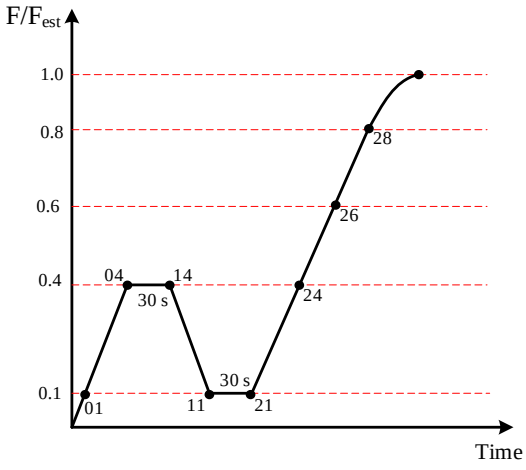

(d) Loading procedure

Figure 3: Test setup and loading procedure.

At the outset of the tests, the mean moisture content in timber block was measured as 14.16%, 12%, and 13%, in the S_1, S_2, S_3 push-out test specimens, respectively.

Using the formulations given in the technical specification BNTEC TS 19103 [40], the failure was predicted to occur due to compressive crushing of the timber with an estimated maximum load (F_{est}) of 188 kN for the specimen containing four connectors. The testing procedure was implemented following the European standard EN 26891 [38]. It is the following: the load was increased to 40% of the maximum estimated load and maintained for 30 s,

then reduced to 10% of the maximum estimated load (F_{est}) and maintained also for 30 s, and finally increased, until a slip of 15 mm was exceeded (see Figure 3(d)).

2.1.3 Material and material tests

A. Timber

Specimens in this study were made of solid pine (Spruce) graded as C24 [34]. In order to determine the actual compressive strength and the actual modulus of elasticity (MOE) of the timber parallel to the grain, nine samples from the same batch, with dimensions of 200 × 75 × 450 mm (width × thickness × length), were subjected to axial load using compression test. The average moisture content was 11.6%, with a standard deviation of 0.5%. Tests were performed according to the European standard EN 408 [36]. The average compressive strength and elasticity modulus were 34.30 MPa and 7152.6 MPa, with a coefficient of variation (CoV) of 9.3% and 22.5%, respectively.

B. Concrete and rebars

The compression tests on concrete were conducted following the European norm EN 12390-3 [37]. For each push-out specimen, six cylindrical concrete samples measuring 110 mm in diameter and 220 mm in length were tested. The compressive strength of concrete and its mean value are provided in Table 1. It should be noted that the push-out specimens were tested at an early age of concrete ensuring that the concrete strength on the day of testing ranged from approximately 60% to 80% of the concrete characteristic strength, as stipulated by Eurocode 4 [56].

For reinforcement of concrete slabs and notched connectors, rebars of B500B grade were used.

Table 1: Concrete strength of push-out tests.

Specimen	*Slab 1*				*Slab 2*			
	Age (days)	f_c [MPa]	f_{cm} [MPa]	CoV	Age (days)	f_c [MPa]	f_{cm} [MPa]	CoV
S_1	7	23.42 24.80 27.13	25.12	7.48%	9	26.21 29.90 26.99	27.70	7%
S_2	8	26.36 25.63 29.10	27.03	6.77%	10	25.59 28.79 24.18	26.19	9%
S_3	9	26.99 28.07 28.86	27.97	3.36%	11	26.18 29.03 25.74	27	6.6%

2.1.4 Test results and discussion

A. Observation and failure mode

The load-slip curves of the push-out specimen containing four connectors are illustrated on Figure 4(a). The slip was measured along the timber grain direction. The test curves show a rigid and linear behaviour before a sudden load drop, declining from 157.6 kN to 142.2 kN, 128.7 kN to 125.2 kN, and 187.43 kN to 180.75 kN, in S_1, S_2, and S_3 tests, respectively (see Figure 4(b)). The load drop occurred following a sudden flat noise heard during the test, which may be attributed to an abrupt timber crushing. Following this, a nonlinear behaviour can be observed until maximum loads (F_{max}: defined as the highest force recorded) of 210.5 kN, 170 kN, and 198.5

kN, attained in S_1, S_2, and S_3 tests, respectively. This behaviour might be attributed by the confinement of the timber inside the concrete. The corresponding mean slips were 2 mm, 2.56 mm, and 1.89 mm, in S_1, S_2, and S_3 tests, respectively. It should be noted that no cracks were observed in the timber panels nor in concrete slabs.

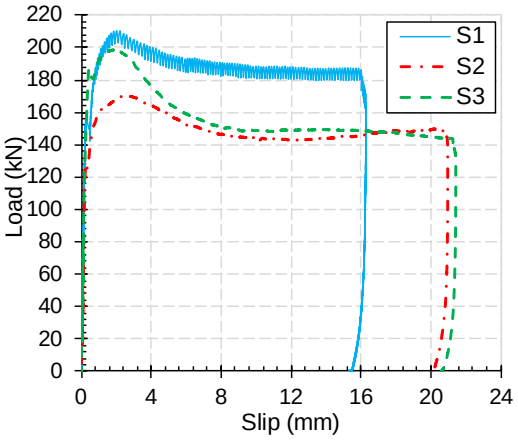

(a) Load-slip curves

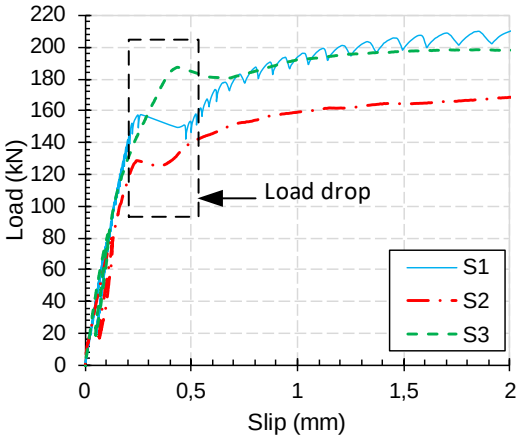

(b) Zoom on load-slip curves

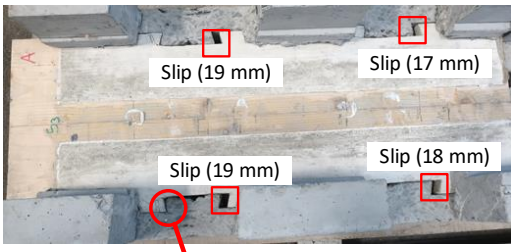

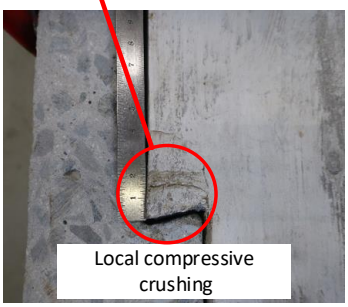

(c) Local timber crushing

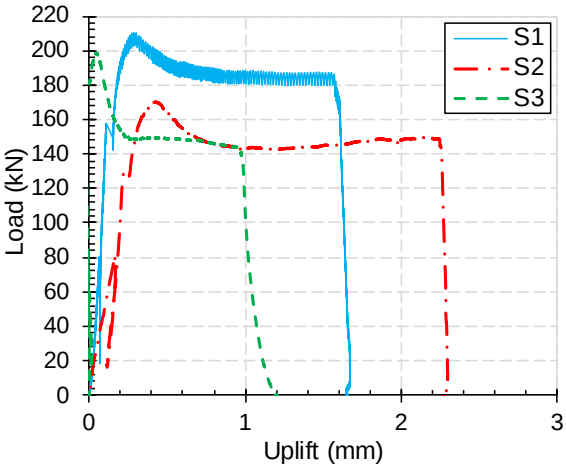

(d) Load-uplift curves

Figure 4: Force-slip and force-uplift curves of the push-out tests.

During the post peak phase of the S_1 test, the load-slip curve showed little fluctuations of loads for an unknown reason (see Figure 4(b)). The maximum slips were 16.28 mm, 20.92 mm, and 21.43 mm, for S_1, S_2, and S_3 tests, respectively. At the end of each test, the specimen was cut to observe the condition of the notches and visualize the deformation of timber around the notched connectors (see Figure 4(c)). At the timber-concrete interface, a local compressive crushing failure along the grain direction of the timber was observed (Figure 4(c)).

The load-uplift curves of the push-out specimen containing four connectors are illustrated in Figure 4(d). When the maximum force was attained, mean uplifts of 0.26 mm, 0.42 mm, and 0.05 mm, were measured in S_1, S_2, and S_3 tests, respectively. The low value of the uplifts might be attributed to the distinctive dovetail shape of the notch connector, which provides a geometrical locking mechanism between timber and concrete layers.

B. Shear stiffness

The guidelines of the standard EN 26891 [38] were used to compute the slip modulus of the notched connector (see Figure 5).

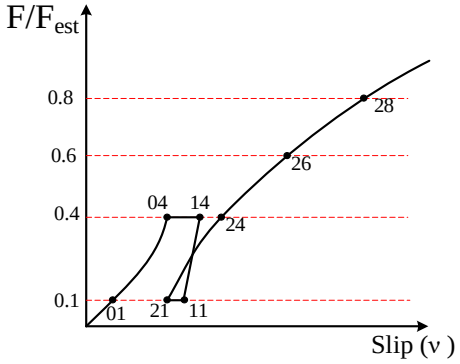

Figure 5: Idealized load-slip curve.

The serviceability shear stiffness (K_s) and the ultimate shear stiffness (K_u) for one connector have been calculated in accordance to the following formulations:

$$K_s = \frac{0.4(F_{est}/4)}{v_{i,mod}} \qquad K_u = \frac{0.6(F_{est}/4)}{v_{0,6} - v_{24} + v_{i,mod}} \tag{1}$$

with

$$v_{i,mod} = \frac{4}{3}(v_{04} - v_{01}) \tag{2}$$

where v_{01}, v_{04}, and $v_{0,6}$ denoted the slip values at forces of $0.1F_{est}$, $0.4F_{est}$, and $0.6F_{est}$, respectively, while v_{24} is the measured slip at the shear load level of $0.6F_{est}$ along the second ramp. The values of K_s and K_u as well as the maximum load capacity of one notched connector are summarized in Table 2. The shear stiffness values derived from S_1 and S_3 tests displayed similarities, whereas in the case of S_2 test, the stiffness was comparatively lower. This could be possibly attributed to the inherent variability of timber, as the behaviour of the connection system is predominantly governed by the compression of the timber. Additionally, the notched connector exhibited a minor degradation in stiffness when transitioning from the service limit state to the ultimate limit state. Despite the limited number of push-out tests, the CoVs of the shear resistance and slip moduli of the connector, being 10.7% and 12.9%, are in good agreement with the experimental CoVs from the timber compression tests (see section 2.1.3).

Table 2: Test results – shear stiffness of one notched connector.

Push-out tests	F_{max} (kN)	K_s (kN/mm)	K_u (kN/mm)
S_1	52.6	189.5	166.5
S_2	42.5	151.1	168.7
S_3	49.6	192.2	168.5
Av. (CoV)	48.3 (10.7%)	177.6 (12.9%)	167.9 (0.7%)

C. *Design value of the shear connector*

The three tested push-out specimens shared an identical configuration and a common failure mode, which was primarily attributed to the local compression of timber around the notched connectors along the grain direction. Consequently, the design value can be determined using the maximum forces obtained from the push-out tests, following the guidelines outlined in Annex D of Eurocode 0 [58]. The design resistance value can thus be formulated as follows:

$$X_d = \eta_d \frac{X_k(n)}{\gamma_m} = \frac{\eta_d}{\gamma_m} m_X(1 - k_n V_X) \tag{3}$$

where X_d is the design value of the studied variable X, which is the connector resistance in this case, η_d is the design value of the possible conversion factor, (equal to 1), γ_m is the partial factor for materials, (equal to 1.3 for timber since the failure was governed by the local compression of timber), n is the sample size, (equal to 3), k_n is the characteristic fractile factor, (equal to 3.37 in case of unknown V_X when 3 tests have been made), V_X is the CoV of the studied variable X, and m_X is the mean value of X. Using the maximum resistance of the connector provided in Table 2, the design value of the connector strength is calculated and given in Table 3.

Table 3: Design value of the shear connector strength.

m_X [kN]	V_X	R_d [kN]
48.25	10.7%	23.72

D. *Comparison and discussion*

Numerous shear connectors are presently available in the literature, with each having its own level of complexity and possessing its own set of advantages and disadvantages. Consequently, a comparative analysis is conducted in this section, specifically comparing the 3D notched connection in this paper with other usual notched connections that have been tested in the literature [33], [41], [42]. To facilitate comparison with the results, the strength and stiffness of connections were commonly normalized to a one-meter width. The normalized stiffness and shear resistance of the notched connectors from the studies in the literature and the present 3D notched connector in this paper are provided in Table 4. It should be noted that for the ductility classification of the notch connection in the present study, the method proposed by Yeoh el al. [42] has been applied.

Djoubissie et al. [33] investigated the shear properties of a triangular notched connection with and without steel reinforcing rod for timber-concrete composite floor. The system was composed of tropical wood, Kosipo (red wood), with an average compressive strength of 55 MPa and a modulus of elasticity of 11190 MPa, and concrete with an average compressive strength of 25 MPa at 28 days after casting. The length, depth, and width of the triangular notch were 92 mm, 40 mm, and 65 mm, respectively. The unreinforced and reinforced notched connectors were denoted as CT and CTS90- HA12, respectively. The CTS90-HA12 connector was reinforced with 150 mm length threaded steel connectors, with a diameter of 12 mm, screwed at an angle of 90° to the grain. The ultimate tensile strength of the steel connectors was 331 MPa. The normalized shear capacity, the serviceability slip modulus, and the ultimate slip modulus of the connector CT obtained from the asymmetric tests were 366 kN/m, 740 kN/mm/m, and 834 kN/mm/m, respectively. For CTS90-HA12, the values were 838 kN/m, 1460 kN/mm/m, and 646 kN/mm/m, respectively. In both configurations, the brittle collapse of the connection was

induced by the concrete shear failure in the notch (see Figure 6(a)). Additionally, it was observed that the CT connector had no ductility, and that the use of mechanical fasteners can enhance the post-peak behaviour.

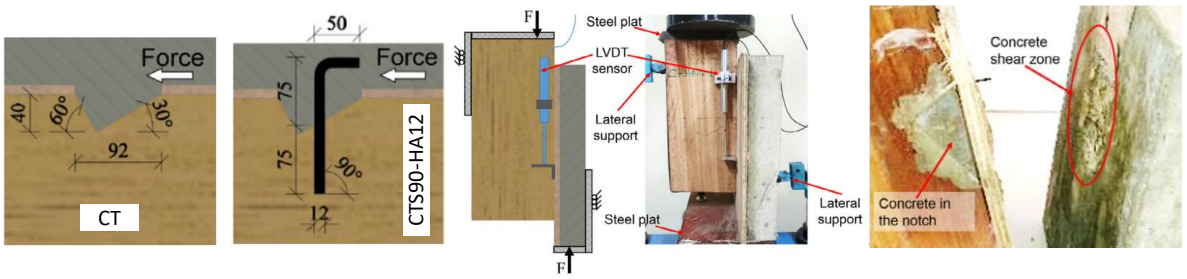

(i) Connectors geometry (ii) Asymmetric push-out test (iii) Failure mode

(a) Djoubissie et al. [33]

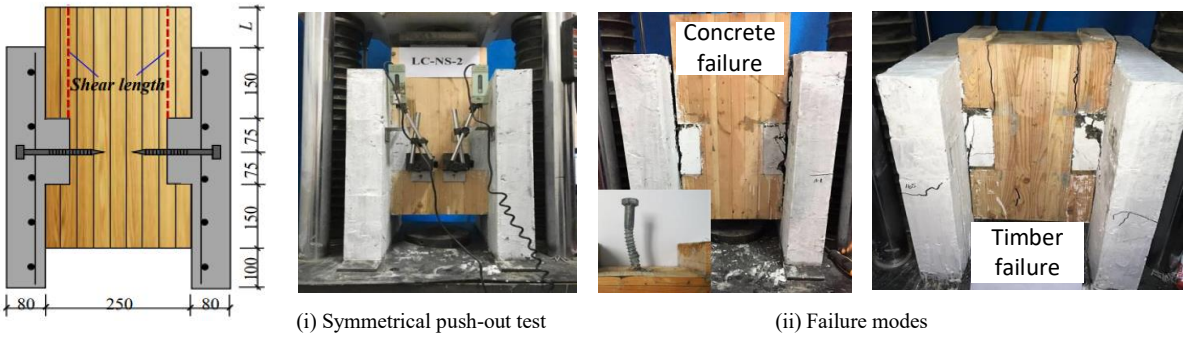

(i) Specimen (i) Symmetrical push-out test (ii) Failure modes

(b) Jiang et al. [41]

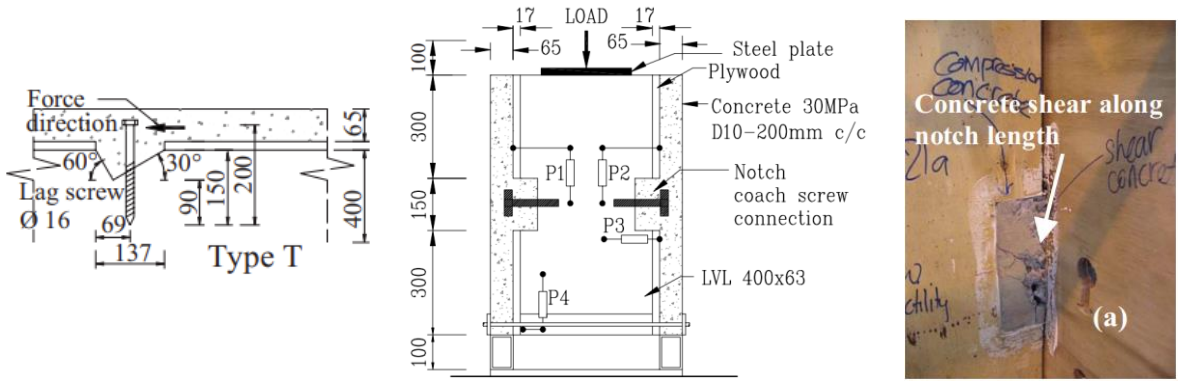

(i) Connectors geometry (ii) Symmetrical push-out test (iii) Failure mode

(c) Yeoh et al. [42]

Figure 6: Notched connector configurations and failure modes.

Jiang et al. [41] performed push-out tests on rectangular notched connectors while considering the concrete type, the shear length of timber, and the reinforcement effects. Timber members were made from Douglas fir with a mean compressive strength and a modulus of elasticity of 43.5 MPa and 10680 MPa, respectively. The average compressive strength of normal and lightweight concrete was 29.2MPa and 28.7 MPa, respectively. The length, depth, width of the notch were 150 mm, 50 mm, and 150 mm, respectively. In case of reinforced connectors, lag screws with a diameter of 16 mm and a length of 200 mm were used. Their yield strength and ultimate tensile strength were 360 and 450 MPa, respectively. The unreinforced notched specimens were named NC-N-1 for normal concrete and LC-N-1 for lightweight concrete. The reinforced lightweight concrete notched specimen was denoted by LC-NS-1. The shear length of timber was 350 mm for NC-N-1 and LC-N-1 configurations, and 150

mm for LC-NS-1 configuration. A symmetrical push-out test was used to determine the shear properties of the connections. Based on their findings, the normalized shear resistance was 535.8 kN/m for NC-N-1, 460.9 kN/m for LC-N-1, and 498 kN/m for LC-NS-1. The normalized serviceability stiffness was 1530 kN/mm/m for NC-N-1, 1562 kN/mm/m for LC-N-1, and 1545 kN/mm/m for LC-NS-1. The failure mode was by shear in the concrete in case of NC-N-1 and LC-N-1 and by shear in concrete or timber for LC-NS-1 (see Figure 6(b)). Among all the connectors, only the LC-NS-1, which failed by shear in concrete, showed a ductile behaviour.

Triangular notched connectors have been studied by Yeoh et al. [42] for LVL-concrete composite beams (see Figure 6(c)). The mean modulus of elasticity of LVL was 11300 MPa. The average compressive strength of low shrinkage concrete was 30 MPa. The length, depth, and width of the rectangular notch were 300 mm, 50 mm, and 63 mm, respectively. The length, depth, and width of the triangular one were 137 mm, 60 mm, and 63 mm, respectively. The notches were reinforced with 16 mm steel lag screw. The normalized shear resistance, serviceability slip modulus, and ultimate slip modulus of the triangular notched connector were 1346 kN/m, 2314 kN/mm/m, and 2203 kN/mm/m, respectively. The tested notched connector had a low ductility, and its collapse was governed by the shear failure of concrete.

The 3D notched connector in this study reached higher shear resistance compared to the unreinforced notched connectors CT, NC-N-1, and LC-N-1, and to the reinforced notched connector LC-NS-1. The shear resistance of the reinforced triangular notched connector T was twice that of the 3D notched connector, possibly due to the larger dimensions of connector T, which was longer and deeper. Regarding stiffness, the 3D connection showed greater stiffness at both SLS and ULS compared with the cited connections, exceeding slightly the T connector without requiring any supplementary mechanical steel fasteners. Concerning the collapse, all the connectors without steel fasteners from the literature discussed in this section experienced brittle failure with low ductility, whereas a better post-peak behaviour was obtained for the connectors with steel fasteners. However, the 3D connector in the present study was able to achieve high resistance, high stiffness, and high ductility without extra steel fasteners. This is attributed to its geometry, which featured mechanical locking to limit the uplift and the three shear planes to obtain the preferable failure mode governed by the compressive crushing of timber parallel to the grain.

Based on push-out test results, the 3D notched connection seems to offer remarkable attributes, such as high strength, significant stiffness, and ductility. Its qualities must however be confirmed by a test of the entire timber-concrete system, that will be presented in the subsequent section.

Table 4: Shear capacity and stiffness of different types of notched connector per one meter width.

Shear connector type *Length × depth × width (mm)*	*Steel reinforcement*	*Shear capacity* F_{max} (kN/m)	K_s (kN/mm/m)	K_u (kN/mm/m)	*Failure mode*	*Ductility*	*Reference*
CT: Triangular notch 92×40×65	(x)	366	740	834	Concrete shear	No ductility	[33]
CTS90-HA12: Triangular notch 92×40×65	(✓)	838	1460	646		Low ductility	
NC-N-1: Rectangular notch with normal concrete 150×50×150	(x)	535.8	1530	-	Concrete shear	No ductility	[41]
LC-N-1: Rectangular notch with lightweight concrete 150×50×150	(x)	460.9	1562	-	Concrete shear	No ductility	
LC-NS-1: Rectangular notch 150×50×150	(✓)	498	1545	-	Concrete shear or timber shear	Low or no ductility	
T: triangular notch 137×60×63	(✓)	1346	2314	2203	Concrete shear	Low ductility	[42]
3D notched connector 116×28×70 mm	(x)	690	2537	2398	Compressive crushing of timber	High ductility	Present study

(x): No steel fasteners. (✓): with steel fasteners.

2.2 Inversed 6-point bending tests

In order to explore the overall behaviour of a full-scale timber-concrete composite beam with the 3D notched connector, six-point bending tests are performed to analyse the bending stiffness, failure modes, mid-span strain distribution, as well as interface slips and uplifts along the beam span.

2.2.1 Specimen of composite beam floor

In the present study, three TCC floors, denoted by F_1, F_2, and F_3, were pre-designed using the γ-method provided in the Eurocode 5 [35] under both serviceability limit state (SLS) and ultimate limit state (ULS) loading conditions. Additionally, the timber cross-section was selected to conform to the recommended height limitations for floors in buildings. In this pre-design phase, the shear stiffness value of the notch connection obtained from push-out tests was adopted (see section 2.1.4), despite variations in concrete strength observed in flexural tests. Consisting of two identical T-shape timber beams embedded in a concrete slab, the composite floor was 920 mm wide and 6850 mm long (see Figure 7(a) and Figure 7(b)). Each T-shape timber beam was linked to the concrete slab using 14 3D ductile-notched connectors symmetrically spaced from mid-span. The groove dimensions were the same as those indicated in push-out tests (see section 2.1.1). The longitudinal distribution of notched connectors is depicted

in Figure 7(b). The concrete slab was reinforced using ST10 steel mesh with 6 mm rebars, spaced at 200 mm intervals in both longitudinal and transverse directions. In turn, the same configuration of the rebars that was used for the push-out specimens was reemployed (see Figure 2(f) in section 2.1.1 and Figure A. 2 in Annex A.). It is worth mentioning that the cross-section of the specimen presented in Figure 8(a) does not include all the rebars placed inside the concrete slab.

In order to reduce friction between materials, the timber beams were painted before specimen casting. In addition, polystyrene blocks were used as a formwork for concrete slab and concrete drops pouring (Figure 8).

A transportation system was employed in order to transport the specimen after concrete casting in factory without pre-damaging the specimen. As depicted in Figure 8, it consisted of two longitudinal IPE-300 steel profiles connected together using four transversal HEA-200 steel profiles. The specimen was connected to the transportation system via four rows of three lifting anchors each (with a diameter of 20 mm), which were installed in the concrete rebars before pouring. The longitudinal spacing between two rows of anchors was 1235 mm, and the transverse spacing between two anchors in the same row was 325 mm. It should be highlighted that each specimen was fabricated using the same concrete class (C25/30) but on a different date, resulting in varying ages and batches of concrete (2.2.4B).

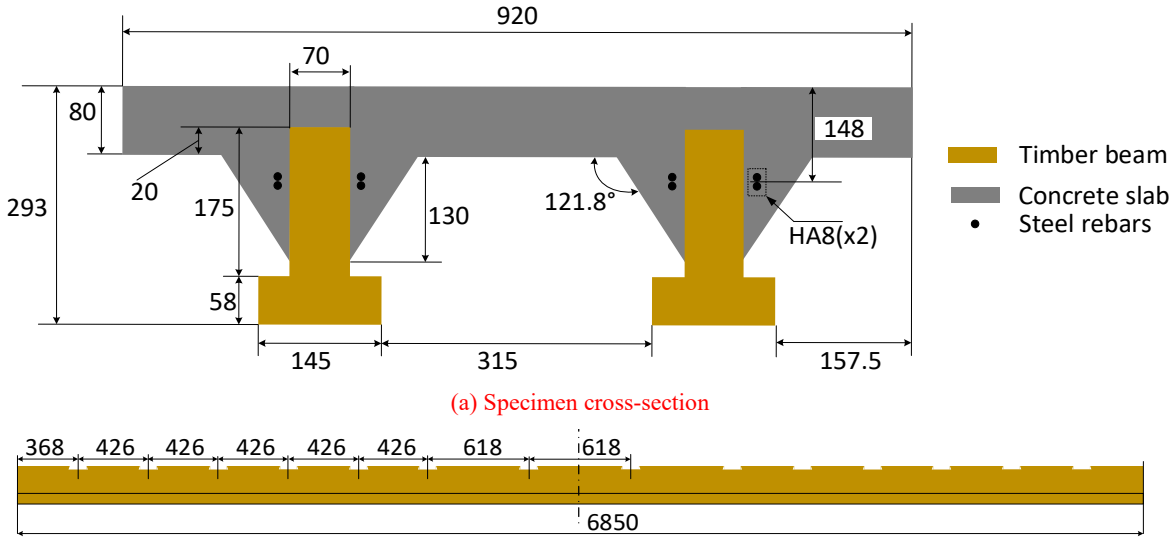

(a) Specimen cross-section

(b) Distribution of notched connectors

Figure 7: Details of timber-concrete composite floor (dimensions in mm).

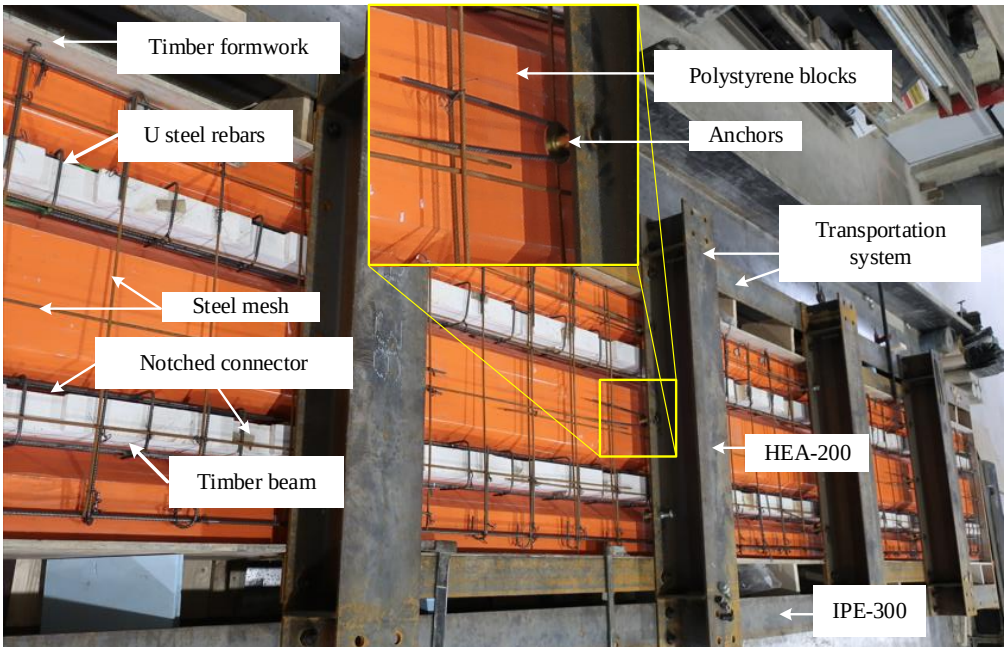

Figure 8: Specimen before casting.

2.2.2 Test setup

In this study, the self-weight of the timber-concrete specimen, G_{slab}, was equal to 2.7 kN/m^2. All the specimens were designed to sustain an additional dead load, (G_{add}), of 2.2 kN/m^2 and a live load, q_k, of 1.5 kN/m^2. The dead load and live load values were calculated in accordance with the European standard EN 1991-1-1 [57] (Category A-floors). The combination of actions at both quasi-permanent serviceability limit state (SLS) and ultimate limit state (ULS) were estimated following the European standard EN 1990-1-1 [58] and are presented in Table 5.

Table 5: Combination of actions at quasi-permanent SLS and ULS.

State	*Partial factors*		*Combination*	*Value* [kN/m^2]
	Permanent actions	Variable actions		
SLS quasi-permanent	1	0.3	$1 \times (G_{slab} + G_{add}) + 0.3 \times q_k$	5.35
ULS	1.35	1.5	$1.35 \times (G_{slab} + G_{add}) + 1.5 \times q_k$	8.86

Additionally, the weight of the testing device, which was initially laid on the specimen, was 1.74 kN/m^2. Consequently, the specimen, under its self-weight (2.7 kN/m^2) and the weight of the testing device, reached 83% of the quasi-permanent SLS (5.35 kN/m^2), potentially leading to a non-negligible initial deflection (see the configuration illustrated in Figure 9(a)). Therefore, to be able to measure accurate deformations and deflections, as well as to determine the initial stiffness, a particular test setup is proposed using an inversed bending configuration (Figure 9(b)). In such a configuration, the specimen was invertedly mounted on the testing device. A loading is then applied by pulling the specimen upward, generating tensile stress on the timber cross-section and compressive stress on the concrete cross-section.

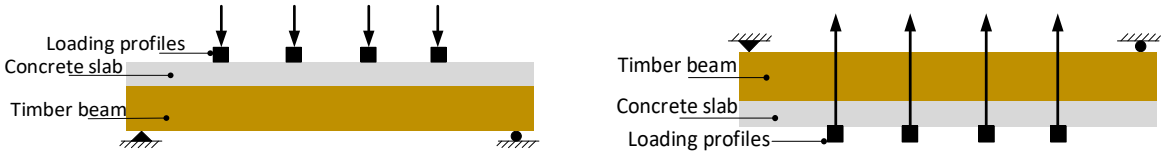

(a) Usual bending test (b) Inverted bending test

Figure 9: Configurations of bending test.

As depicted in Figure 10 and Figure 11, the test setup consisted of a 1500 kN hydraulic jack fixed on a rigid frame, a spreading system that enabled the applied load to be transmitted to the specimen via four points, a transversal guidance system, and two supporting systems. The details of these components are illustrated in Figure 12. Each end of the guiding system (IPE-300 steel profile) was assembled to a U-shaped steel plate by two M18 bolts. Each M18 bolt passed through a 100 mm slotted hole (see Detail 1). The friction between the guiding system and the U-shaped plate was reduced by two PTFE layers. In turn, each U-shaped steel plate was fixed on the rigid frame by six M16 bolts. The hydraulic jack, the steel profile HEB-240 of the spreading system, and the guiding systems were assembled together using four M20 steel rods (see Detail 2). The upper part of the spreading system consisted of one HEB-240 steel profile, four UPN-220 profiles, and four HEA-200 profiles, which were hinged together using bolts with a diameter of 26 mm (see Detail 3). It was designed to equally transfer the load to each of the HEA-200 steel profiles placed directly over the timber beams. The upper and lower parts of the spreading system were assembled together using M20x500 mm steel rods (see Detail 4). Sufficiently long steel rods were used so that the upper steel profiles (HEA200) were no longer in contact with the timber beams when the specimen was lifted by the hydraulic jack. The supporting systems consisted of two roller supports (see Detail 5) and two pinned supports (see Detail 6).

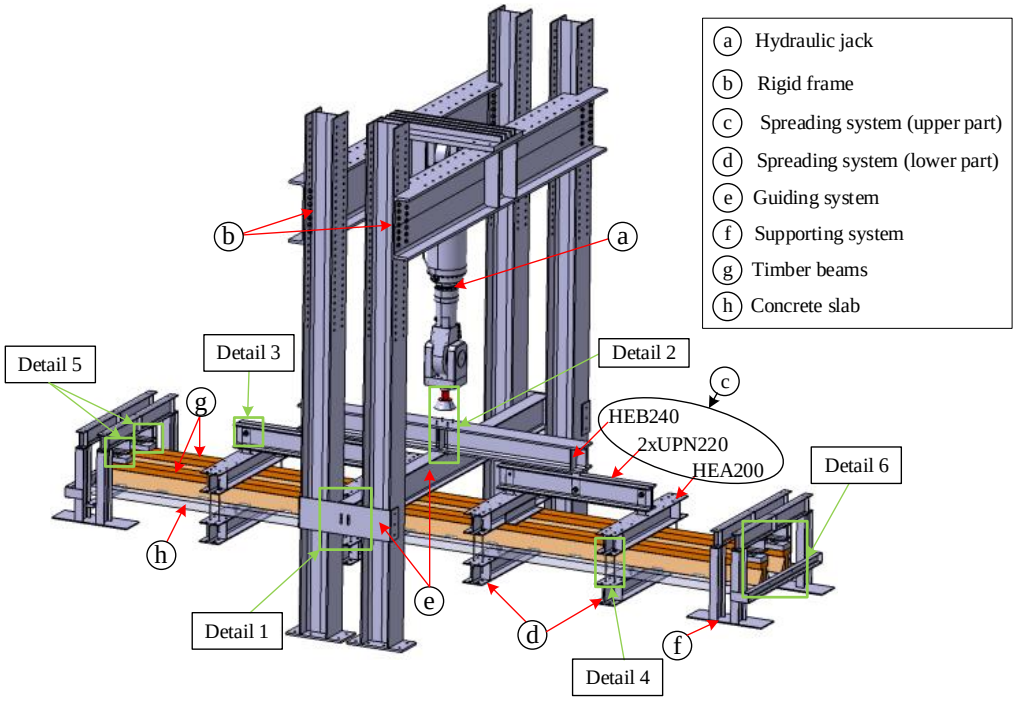

Figure 10: Schematic illustration of the testing device.

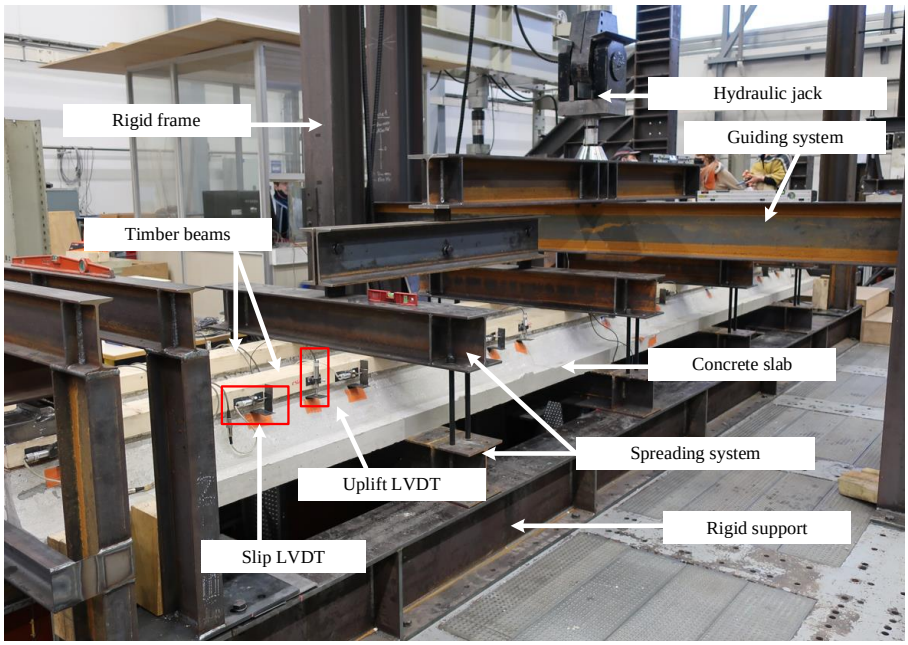

Figure 11: Photograph of the testing device.

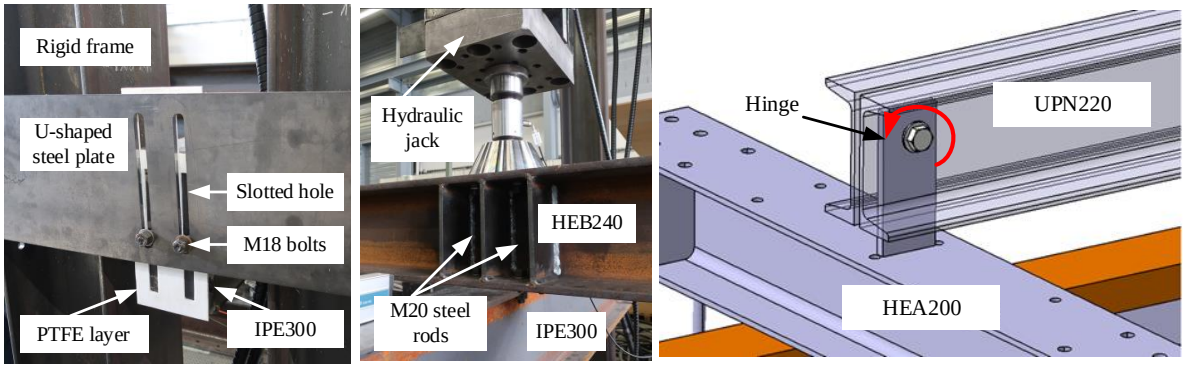

Detail 1 Detail 2 Detail 3

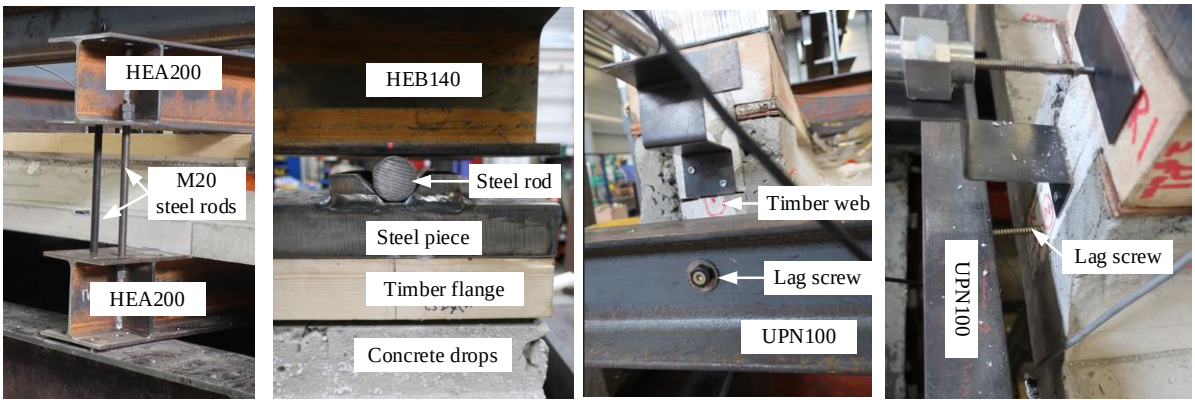

Detail 4 Detail 5 Detail 6

Figure 12: Details of the testing device.

2.2.3 Loading procedure and instrumentation

Conventionally, the European standard EN 26891[38] (see Figure 3(d) in section 2.1.2) for timber-timber connections was adopted to investigate the flexural performance of timber-concrete composite beams [47], [48], [49], [50], [51], [52], [53], [55]. In the current study, a loading protocol inspired from the European standard EN 1994-1-1 [56] was chosen. Supplementary cycles of loading around the estimated SLS level were added, in order to reduce the friction effects and ensure a smooth contact between timber and concrete, see Figure 13. It should be noted that the load values depicted in Figure 13 can be computed by multiplying the values provided in Table 5 by the surface of the specimen (6.55 m × 0.92 m) and adding the self-weight of the specimen as well as that of the spreading system (26-28 kN).

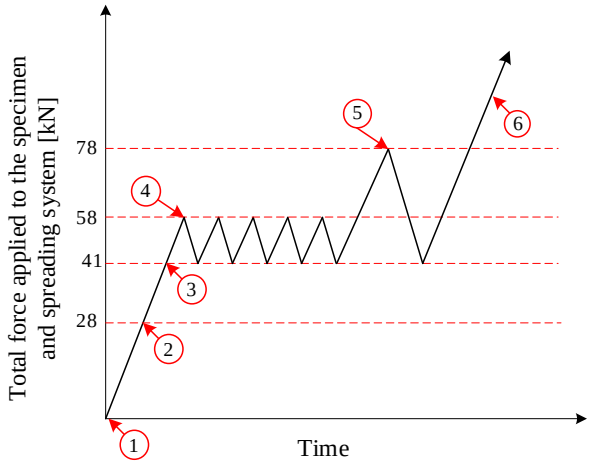

Figure 13: Loading procedure for test F_1.

The load is applied through the hydraulic jack using displacement control protocol. The protocol is divided into six sequential phases: (1) the specimen is initially positioned at its test position; (2) the specimen is lifted without making contact with the supporting systems, and the verification of the combined weight of the specimen and the spreading system is made (26-28 kN); (3) the flanges of the timber beams arrive in contact with the supports at an estimated load level (41 kN, 48 kN and 43 kN, for F1, F2 and F3, respectively); (4) five cycles are made at quasi-permanent service limit state (58 kN); (5) one cycle is performed at ultimate limit state (78 kN); (6) loading is continued up to failure. It should be highlighted that once the specimen was lifted, the upper part of the spreading system was no longer in contact with the flanges of the timber beams, allowing uplift to occur between concrete slab and timber beams throughout the test. During the whole process, the load was applied at a speed of 3 mm/min.

Concerning the instrumentation, five LVDTs, denoted by D_1-D_5, were positioned below the concrete slab along the span to capture the vertical deflection of the tested specimen. The LVDTs D_1 and D_5 had a stroke length of 100 mm, whereas D_2, D_3, and D_4 had a stroke length of 250 mm. For the relative slips between the timber and the concrete, twenty LVDTs were arranged horizontally along the beam. Ten of them were placed on the front side (S_1-S_{10}), while the remaining ten were located on the backside of the tested specimen. The LVDTs S_1-S_4 and S_7-S_{10} had a stroke length of 25 mm, whereas S5 and S6 had a stroke length of 100 mm. The longitudinal positions of slip LVDTs are provided in Figure 14(a). To quantify the uplift between timber and concrete layers, ten vertical LVDTs, denoted by U_1-U_5, were used. Five of them were positioned of the front side, while another five were attached to the backside of the beam specimen (see Figure 14(a)). The LVDTs U_1, U_4, and U_5 had a stroke length

of ± 2.5 mm, whereas U_2 and U_3 had a stroke length of 25 mm. Both uplift and slip LVDTs were attached to the timber beams and the pushrods were set in contact with steel plates that were glued on the concrete side. Besides, fifteen strain gauges were placed at the mid-span of the composite beam to capture the strain profile across the cross section. Among these, three were positioned on the concrete slab, four on the steel rebars, and eight on the timber beams, as illustrated in (Figure 14(b)).

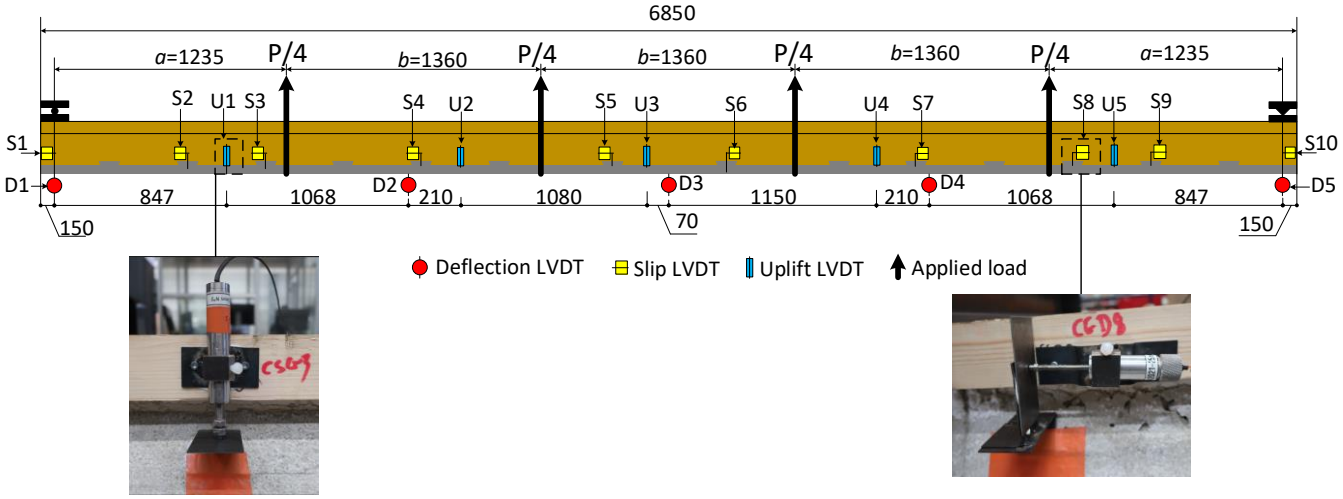

(a) LDVTs distribution along the beam span.

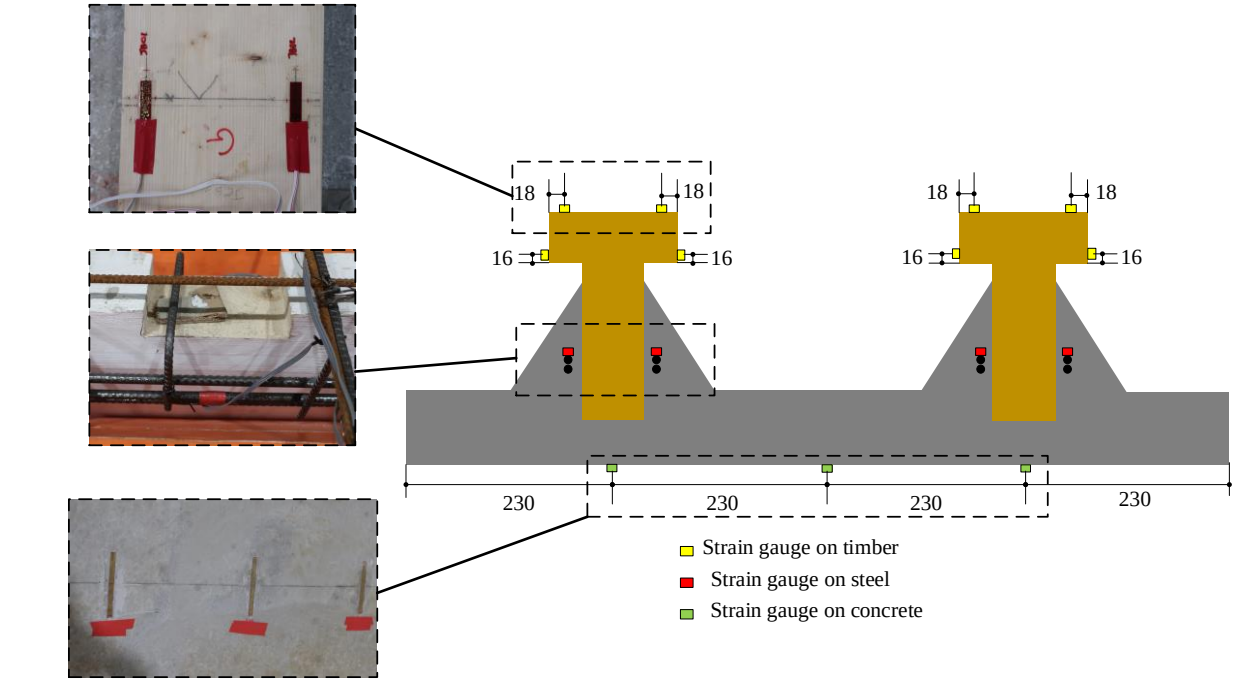

(b) Strain gauges arrangement at the beam mid-span.

Figure 14: Layout of measuring instruments (dimensions in mm).

2.2.4 Material properties

A. Timber

The wood used in this test was C24 grade solid pine (Spruce), and the beams were fabricated by France Poutres [59]. To obtain the mechanical properties of the timber, thirty samples were prepared, with ten each for

compression, tension, and flexural tests. The tests were performed according to the European norm NF EN 408 [36]. The compressive samples were 397 mm × 173 mm × 67 mm (height × width × thickness), and tensile samples had a dog-bone shape, measuring 50 mm × 10 mm × 10 mm, in gauge length, width, and thickness. The beam specimens, subjected to 4-point flexural test, had a span of 4350 mm and a T cross section of 175 mm × 68 mm (height × width) for the web and 58 mm × 145 mm (height × width) for the flange. It should be noted that the flange and the web of the timber beam were glued together. Compressive and tensile tests were conducted along the grain direction. In the compressive, tensile, and bending specimens, the average moisture contents were measured as 11%, 11.8%, and 16.4%, respectively. The measured mean compressive, tensile, and flexural strengths were 30.67 MPa, 64 MPa, and 27 MPa, with corresponding coefficient of variations of 6.7%, 17.2%, and 11.1%, respectively (see Table 6). The compressive modulus of elasticity (MOE) and local flexural MOE were 5297.5 MPa and 10400 MPa, with corresponding coefficient of variations of 15.7% and 13.9%, respectively.

Table 6: Mechanical properties of timber.

Characterization test	Specimens number	Mean moisture content	Mean strength [MPa]	CoV
Compression	10	11%	30.67	6.7%
Tension	10	11.8%	64	17.2%
Bending	10	16.4%	27	11.1%

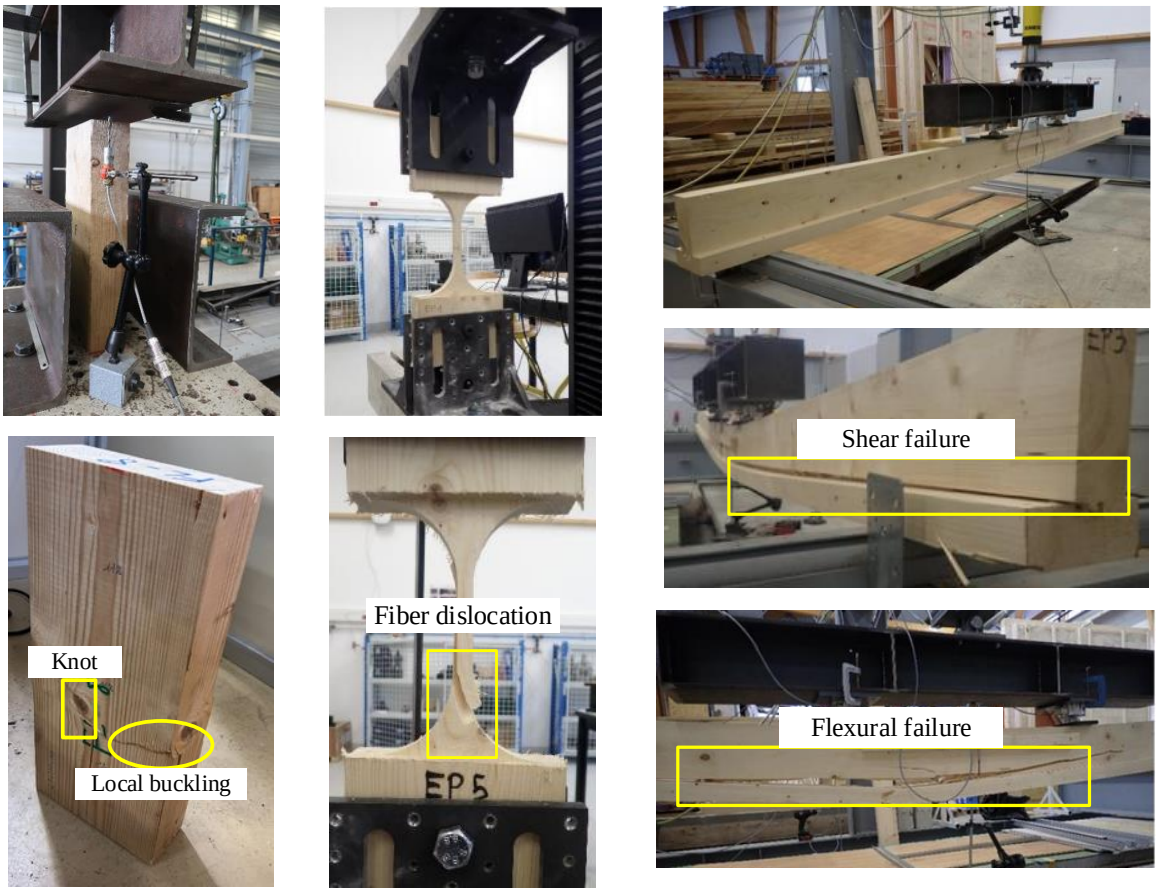

(a) Compression test (b) Tension test (c) 4-point flexural test

Figure 15: Test setup for timber compression, tension, and flexural tests.

In all cases, timber showed a heterogeneous behaviour provoked by the presence of knots and deviations in fibres. In compression tests, the prevalent failure mode was characterized by localized buckling near knots (see Figure 15(a)). Brittle failure modes were observed in the tensile tests, which were caused by the fibre dislocation along the grain direction (Figure 15(b)). During bending tests, two mechanisms of failure were observed: (1) shear failure of the web-flange junction along the beam span; (2) flexural failure, when the flange and web exhibited tensile and compressive failures, respectively (see (Figure 15(c)).

B. Concrete and rebars

During the casting of each timber-concrete specimen, three cylindrical samples (diameter 110 mm, height 220 mm) were made and investigated for their compressive strength on the same day as the bending test. The compressive tests were performed according to EN 12390-3 [37]. The average compressive strengths of concrete of F_1, F_2, and F_3 tests were 25.3 MPa, 47.8 MPa, and 23.3 MPa, with corresponding coefficient of variations of 0.6%, 8.3%, and 15.1%, respectively (see Table 7). The norm NF EN 1992-1-1 [44] was used to estimate the compressive modulus of elasticity of concrete. The estimated MOE were 29052 MPa, 35159 MPa, and 28294 MPa, respectively.

Table 7: Mechanical properties of concrete tested on the day of each flexural test.

Test	*Age* (days)	f_c [MPa]	f_{cm} [MPa]	*CoV*
F_1	27	25.4 25.1 25.3	25.26	0.6%
F_2	43	52.2 44.4 46.8	47.8	8.3%
F_3	92	25.1 25.5 19.2	23.26	15.1%

For the reinforcement, rebars of B500B grade were employed. From tensile tests conducted according to NF EN ISO 6892-1 standard [45] on six dog-bone samples (gauge diameter 8 mm, gauge length 307 mm), the mean yield strength $R_{p0.2}$, mean tensile strength R_m, and mean Young's modulus E were measured as 552.7 MPa, 619.6 MPa, and 197.8 GPa, respectively, with corresponding coefficient of variations of 0.72%, 0.59%, and 1.2% (see Table 8).

Table 8: Mechanical properties of steel used for concrete reinforcement.

Mechanical properties	$R_{p0.2}$[MPa]	R_m[MPa]	E[GPa]
Mean value (CoV)	552.7 (0.72%)	619.6 (0.59%)	197.8 (1.2%)

2.2.5 Results and discussion

A. Load-deflection response and failure mechanism

The starting point is determined by performing a correction of the load-deflection curve obtained from bending test using the approach as presented in Figure 16. In this approach, a secant line was drawn between the fully contact level and the maximum load reached during the 1st SLS cycle and extended to the horizontal line at the load level of the self-weight of the specimen and the spreading system. Then, the intersection point is chosen as the starting point. Finally, the load-deflection curve illustrated in Figure 17 is obtained by shifting the curve with the coordinate of the intersection (in Figure 16) point to the origin point (0, 0).

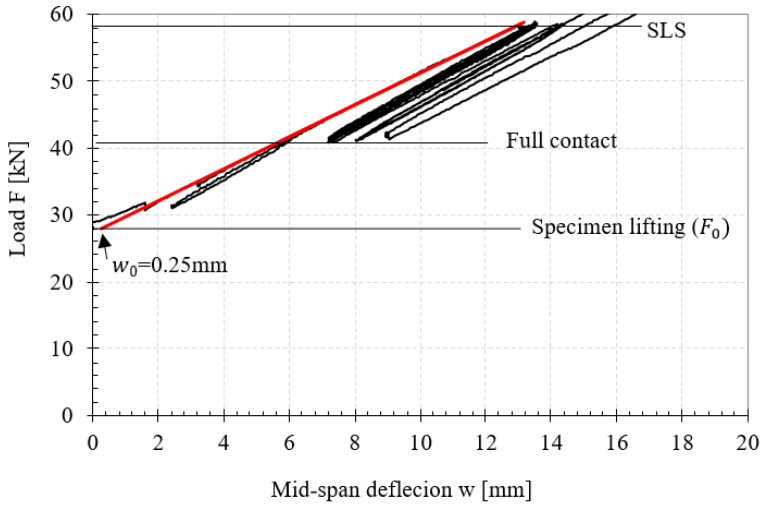

Figure 16: Resetting the force-deflection curve of F_1 test.

The relationship between the vertical pull, F, applied on the specimen and the mid-span deflection, w, obtained from the tests is illustrated in Figure 17. The force F is calculated by subtracting the combined dead loads of the specimen (17 kN) and the spreading system (11 kN) from the total applied load by the hydraulic jack.

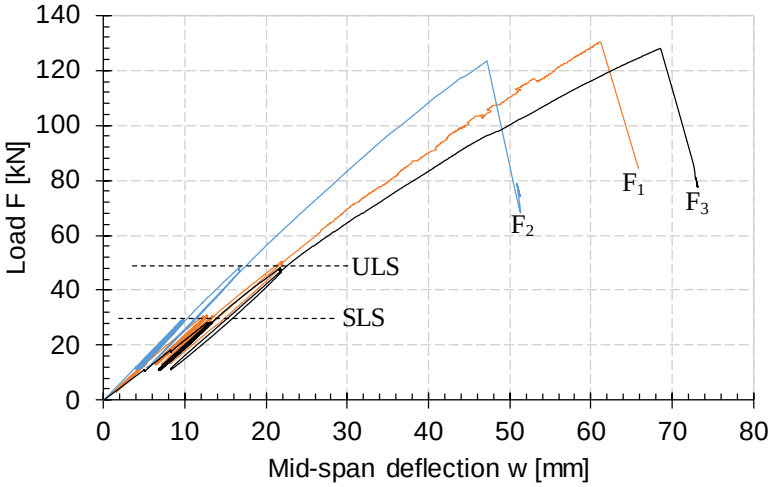

Figure 17: Load-deflection response of the composite beam specimens.

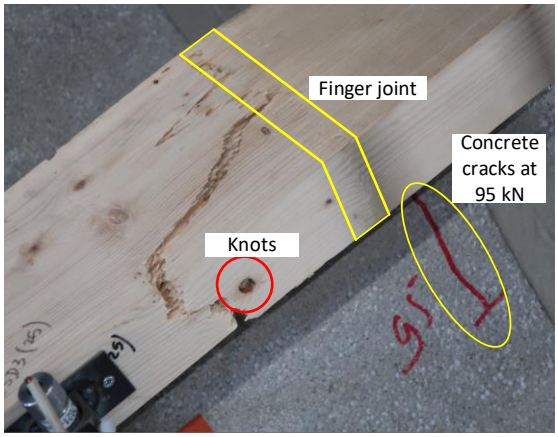

(a) F_1 test

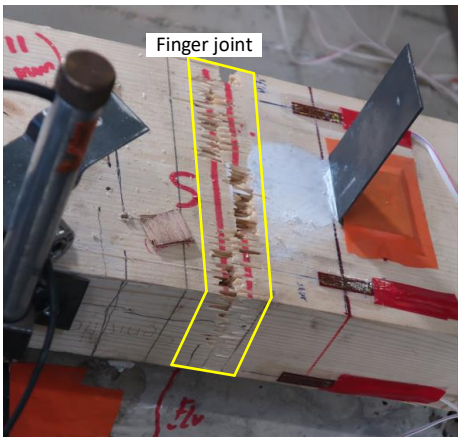

(b) F_2 test

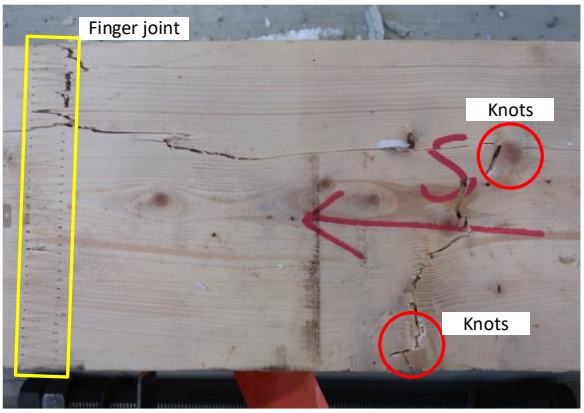

(c) F_3 test

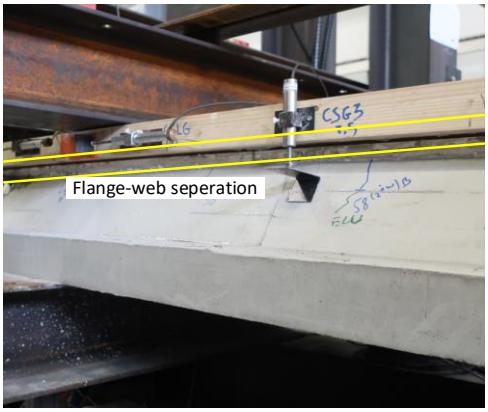

(d) Flange-web separation in timber beam

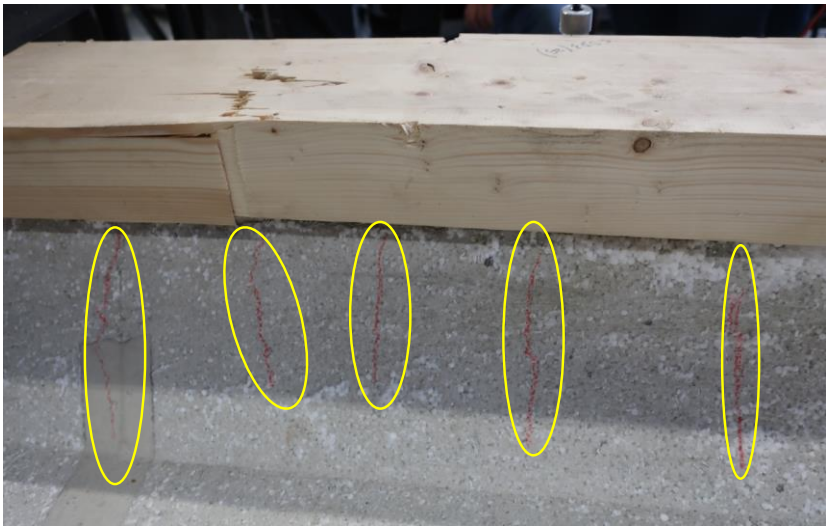

(e) Cracks in concrete drops after failure of F1 test.

Figure 18: Failure mode of timber-concrete specimens.

During the cycling procedure at the quasi-permanent service limit state (SLS), no observable cracks were detected in either the timber beams or concrete slab of the three test specimens. At ultimate limit state (ULS), imperceptible fibre breakage in wood was audibly detected, and fractures became visible on the concrete drops of F_1, F_2, and F_3 tests. However, up to ultimate limit state, a quasi-linear behaviour can be observed.

During the progressive loading process up to the total collapse, the force-deflection curve started to be slightly non-linear, ended by a brittle failure upon reaching the maximum load. The collapse occurred around mid-span in the flange of the timber beam, which was subjected to the highest level of tensile stresses. The rupture location was influenced by the existence of knots and finger joints within the timber beams (see Figure 18(a), Figure 18(b), and Figure 18(c)). Following the collapse, a longitudinal separation between the web and the flange of the timber beams was observed in all tests (Figure 18(d)). The cracks in concrete drops following the collapse of the F_1 test are illustrated in (Figure 18(e)).

B. Bending stiffness and cycling effects

During the bending tests, several cycles have been applied to the specimen in order to reduce the friction at the timber-concrete interface. This cyclic loading can also produce a ratcheting effect if the repeated high contact forces produce an evolutive damage on the materials. In the following, the evolution of tangent and secant stiffnesses during the cycles is studied, to set in evidence these effects and evaluates if a stabilized state is achieved after the five SLS cycles. The tangent stiffness is merely linked to friction effects, while the secant one is influenced by all phenomena.

By considering a simply supported beam subjected to a 6-point flexural test, the experimental bending stiffness, denoted by $(EI)_{exp}$, can be evaluated by employing Eq. (4):

$$(EI)_{exp} = \frac{\Delta F}{96\Delta w}[a(3L^2 - 4a^2) + 3(a+b)L^2 - 4(a+b)^3] \quad (4)$$

where a is the distance from the loading point to the support, a = 1235 mm; b is the distance between two loading points, b = 1360 mm (see Figure 14(a)); L is the beam span, L = 6550 mm. We denote $k = \frac{\Delta F}{\Delta w}$ the slope of a specific cycle in the force-deflection curves to compute the secant stiffness (see Figure 19(a)) and tangent stiffness (see Figure 19(c)).

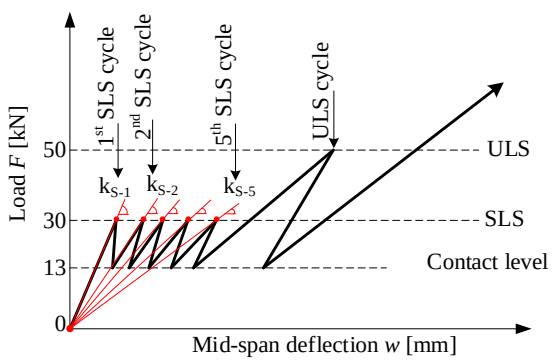

(a) Slope degradation due to the global effects

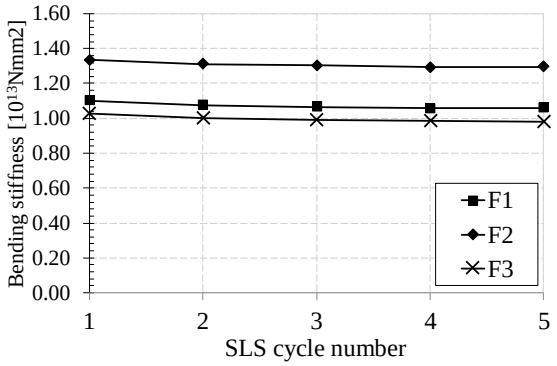

(b) Flexural stiffness degradation due to the global effects

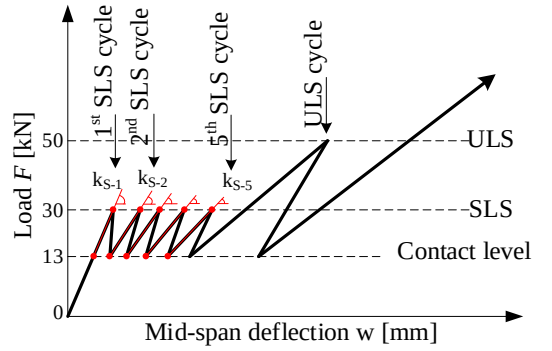

(c) Slope degradation due to merely friction effect

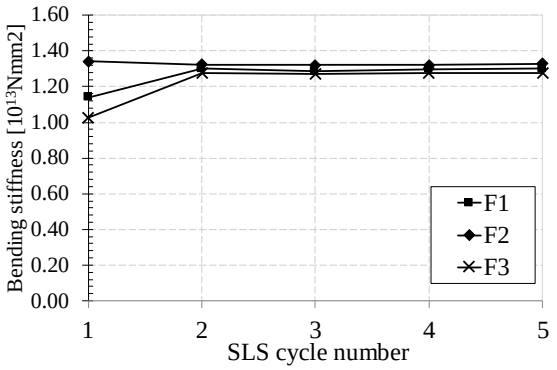

(d) Flexural stiffness degradation merely due to friction effect

Figure 19: Bending stiffness of the tested specimens.

For the secant stiffness, the slope of the force-deflection curves was computed between 0 kN and 30 kN, at SLS level, following the instructions provided in Figure 19(a). Based on the results shown in Figure 19(b), it can be observed that the flexural stiffness seemed to stabilize at the fourth SLS load-unload cycle with corresponding degradations of 3.6%, 3%, and 4.4%, in F_1, F_2, and F_3 tests, respectively. This decreasing is thus small although not negligible.

In order to investigate separately the effects of the friction between the timber and the concrete layers on the flexural stiffness of the composite system, the tangent stiffness of the force-deflection curves is thus computed for each cycle between 13 kN and 30 kN, following the instructions provided in Figure 19(c). The Figure 19(d) illustrates the degradation of the flexural stiffness of the composite system induced by the friction loss between the timber and the concrete. Starting from the 2nd cycle onwards, the flexural stiffness remained nearly constant, indicating the negligible effect of the friction loss on the system. This is unsurprising, given that the timber beams were coated with paint to reduce the friction between the two materials.

Based on the results, it can be concluded that the cycles are useful to provoke the small, but non-negligible, degradation that occurs at the contact interface between materials. Friction effects in this study are negligible, but this may be due to the painting applied on the timber, and this conclusion may not be extended to cases without paint.

C. *Interfacial relative slip data*

Figure 20 and Figure 21(a) show the relationship between the applied load and the relative slip recorded along the beam span at the interface between timber and concrete. The tests showed that the maximum slips were recorded at both ends of the specimen. At service and ultimate limit states, the relative slip was very small. As the applied load increased, the relative slip raised progressively and reached values between 0.7 mm and 2 mm when the specimens collapsed. These values of slips are lower than the mean slip corresponding to the maximum force obtained in the push-out tests (2.34 mm). This indicates that in all the flexural tests, the connectors have not reached the failure load yet. This was confirmed later by the cuts made in the tested specimens to investigate the damaging of the notched connectors (see Figure 21(b)).

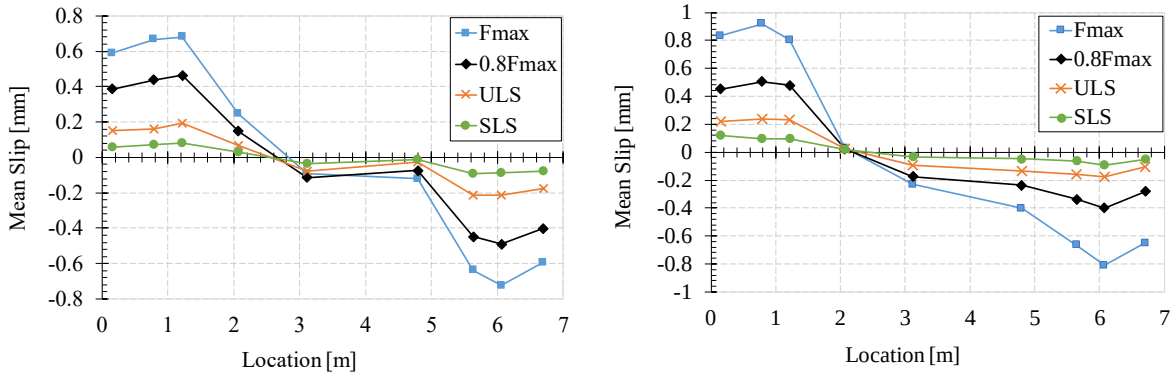

(a) F_1 test (b) F_2 test

Figure 20: Slip values along the length of specimens of the tests F_1 and F_2.

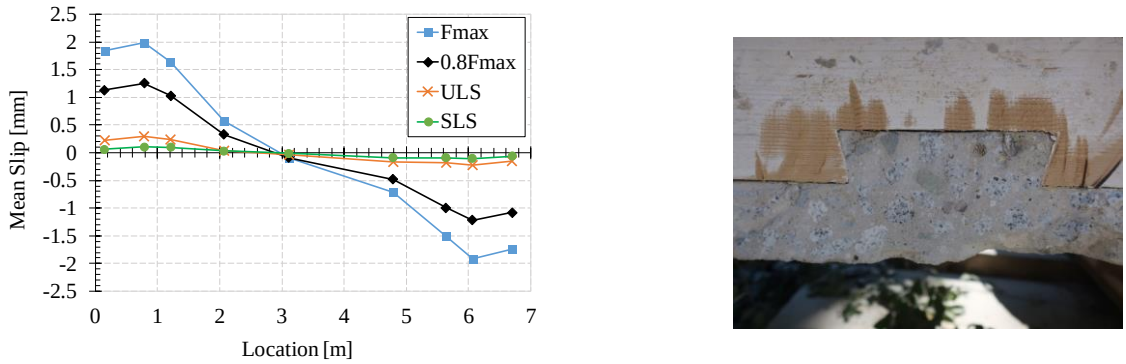

Figure 21: (a) Slip values along the length of specimen of the test F_3. (b) Connector after TCC collapse.

D. *Interfacial relative uplift data*

Figure 22 depicts the relationship between the applied load and the relative uplift measured along the beam span at the timber-concrete interface. The maximum uplifts were recorded at the mid-span of the specimens. At service and ultimate limit states, the relative uplift remained minimal, ranging from 0.05 mm to 0.22 mm. As the applied load increased, the relative uplift increased to reach values between 0.28 mm and 0.5 mm upon the specimen's collapse. Nevertheless, the relatively low uplift values demonstrated the effective geometrical locking provided by the connection's shape, obviating the necessity for additional mechanical fasteners.

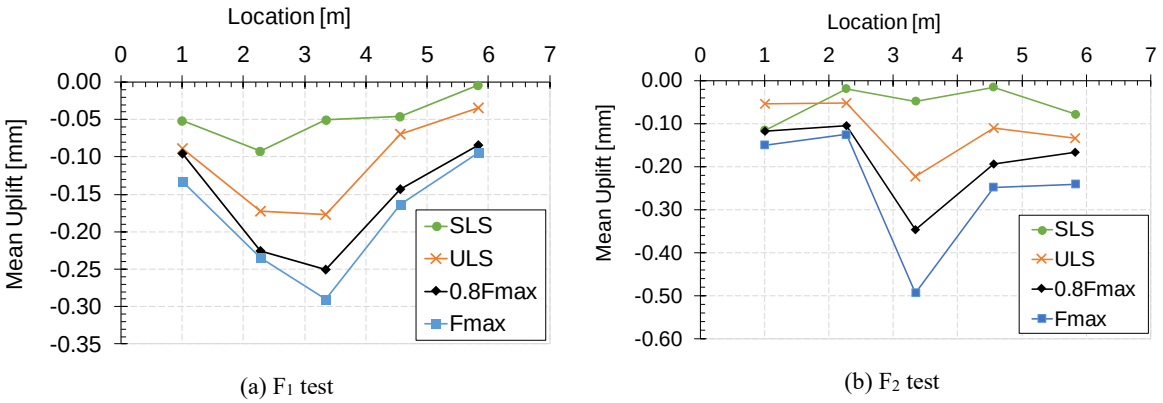

(a) F_1 test

(b) F_2 test

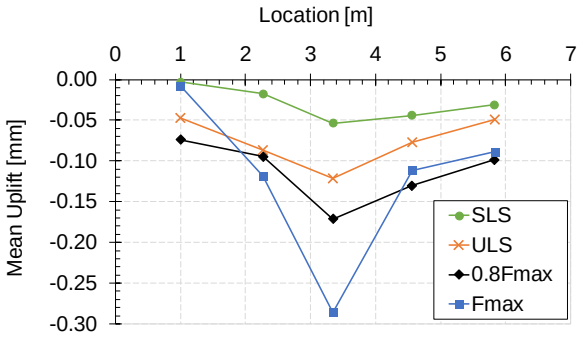

(c) F_3 test

Figure 22: Uplift values along the length of specimens.

E. Strain distribution at mid-span

Figure 23 illustrates the measured strain profiles in the composite section at mid-span for different loading levels. The mean value of the strains measured at the same height was computed. The dashed and continuous lines correspond to the strain profiles in the concrete and the timber cross-sections, respectively. It should be noted that the profiles of the timber section are extended up to the height of the rebars to observe the effect of the slips between the timber and the concrete. Based on the results from tests F_1 and F_3, it is observed that at both serviceability and ultimate limit states the strain distribution seems to be almost linear and continuous from the timber to the concrete cross-section. This confirms that the present notched connection is stiff, allowing to achieve a full degree of shear connection for the TCC floor system. In addition, the slops of both concrete and timber strain distributions are almost the same, the hypothesis of the same curvature of the timber and concrete cross-sections can be then assumed. It should be notice that this hypothesis is postulated by the γ-method, which will be described later in section 3. In test F_2, the discontinuity of strain distribution across the composite section is more noticeable. Moreover, the slopes of both concrete and timber strain distributions are relatively different. Such an effect should be linked to relatively large uplifts between the timber and concrete cross-sections observed in test F_2. It is worth recalling that the concrete strength in test F_2 is almost twice of the ones used in tests F_1 and F_3. This large difference in concrete strength may contribute to the inconsistencies between tests F_1, F_3 and test F_2. Besides, one can suggest that these inconsistencies with tests F_1 and F_3 might come from the errors of measurement of the strain gauges in test F_2.

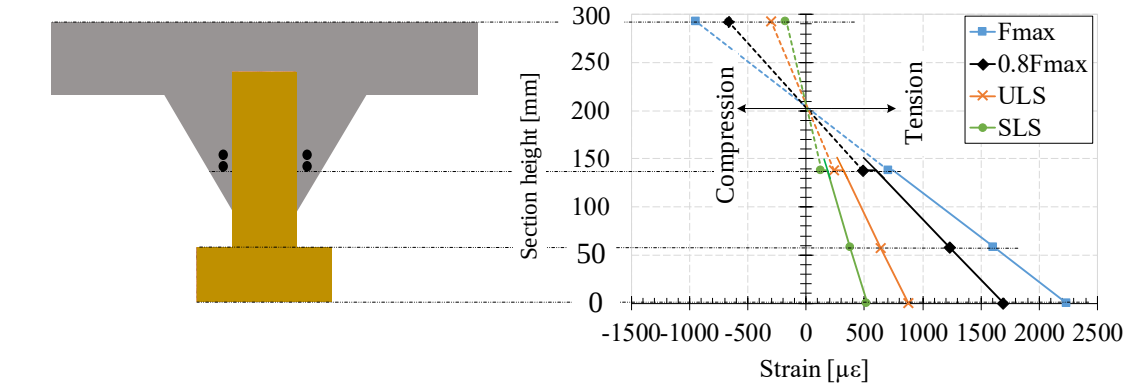

(a) F_1 test

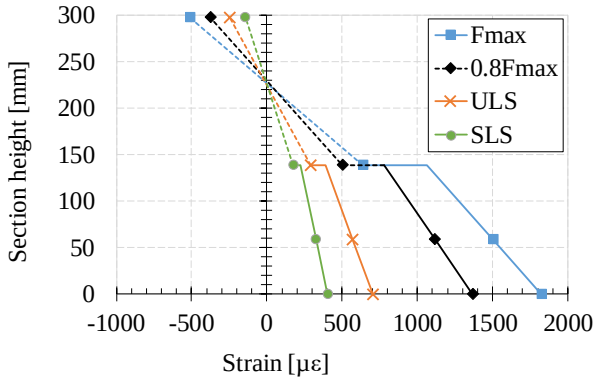

(b) F_2 test

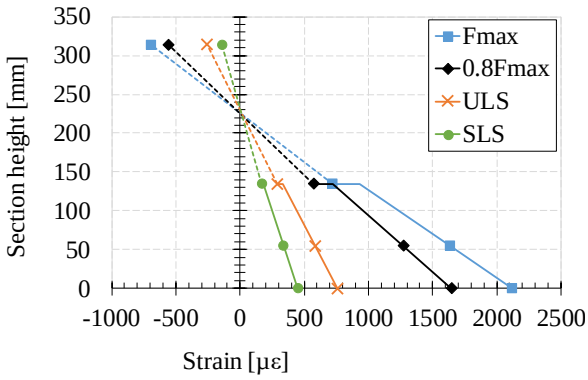

(c) F_3 test

Figure 23: Longitudinal strain profiles at mid-span of the tested specimens.

Based on the measured strains, the stresses in both concrete and timber cross-sections were computed by using the elastic modulus given in section 2.2.4. They are illustrated in Figure 24. It can be observed that at both SLS and ULS, neither the wood nor the concrete has yet reached its yield limits. Furthermore, the neutral axis of the concrete cross-section is found close to the bottom surface of the concrete slab.

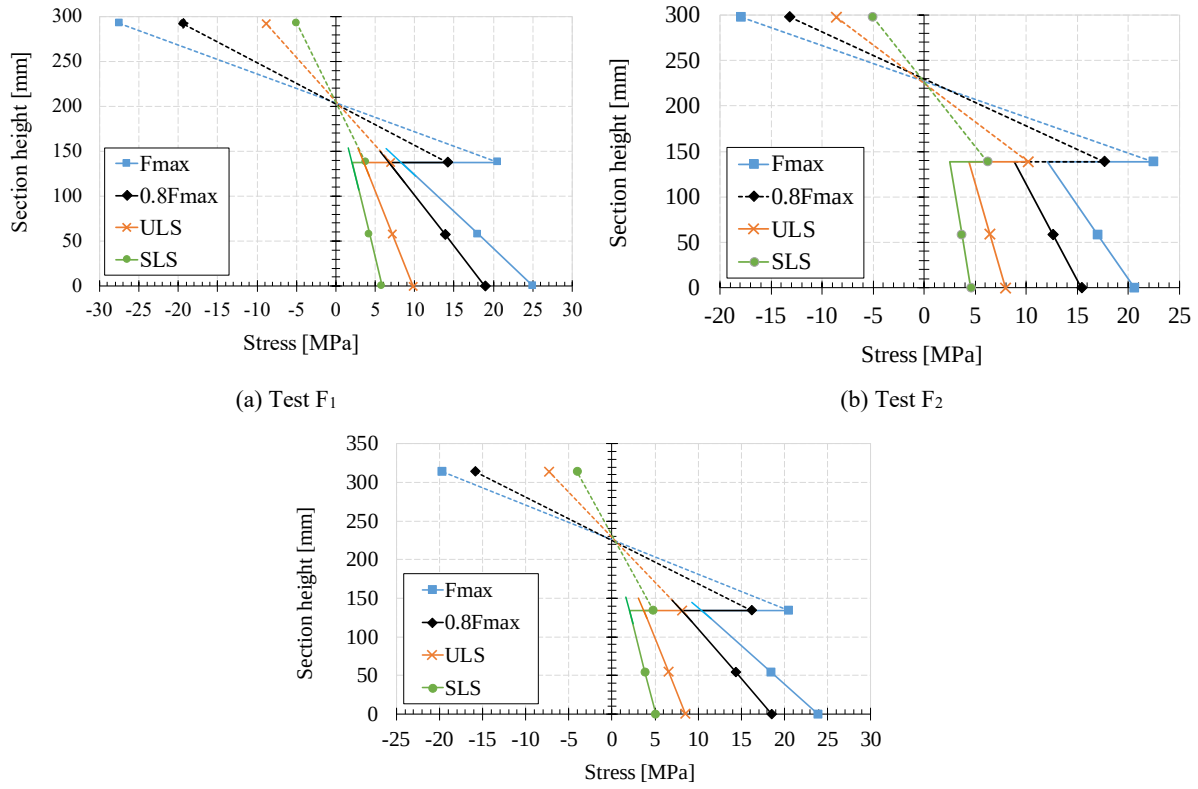

(a) Test F_1 (b) Test F_2

(c) Test F_3

Figure 24: Longitudinal stress profiles at mid-span of the tested specimens.

3. Analytical study

3.1 Introduction

In the context of calculation and design of mechanically jointed timber beams, a simplified method called 'γ-method' was widely adopted. This method is also often chosen to estimate the effective bending stiffness of TCC beams (e.g. [43] and [46]). By considering linear elastic behaviour for the timber, concrete, and shear connections, and assuming that the sectional curvature of both concrete and timber layers is identical, the effective bending stiffness $(EI)_{eff}$ can be expressed as:

$$(EI)_{eff} = \sum_{i=1}^{2} \left(E_i I_i + \gamma_i E_i A_i a_i^2\right) \tag{5}$$

In this formula, E_i, I_i, and A_i denote the elastic modulus, the second moment of area, and the cross-section of the concrete slab ($i = 1$), and timber beam ($i = 2$), respectively, a_i represents the distance between the centroid of the composite member and the centroid of part (i) (see Figure 25), given in Eq. (6), Eq. (7), and Eq. (8):

$$a_1 = \frac{\gamma_2 E_2 A_2}{\sum \gamma_i E_i A_i} d_{1-2} \tag{6}$$

(7)

$$a_2 = \frac{\gamma_1 E_1 A_1}{\sum \gamma_i E_i A_i} d_{1-2}$$

$$d_{1-2} = z_2 - z_1 \quad (8)$$

where d_{1-2} is the distance between the centroids of the two components, z_1 and z_2 represent the distances from the upper surface of the concrete slab to the centroid of the concrete and of the timber cross-sections, respectively, and γ_i is the factor that takes into account the degree of composite action, defined in the range 0 (no composite action) to 1 (full composite action).

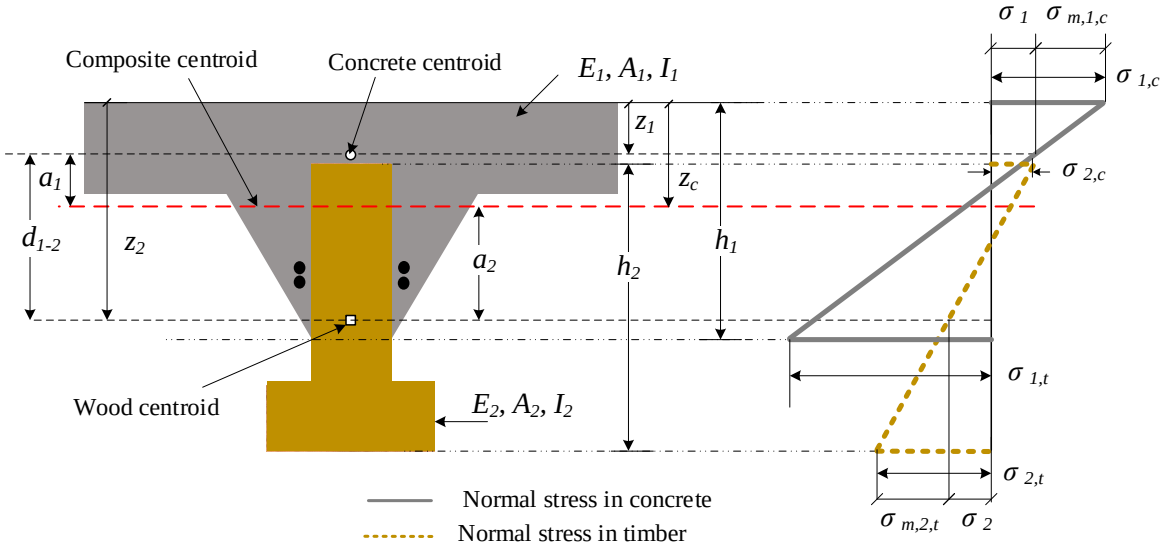

Figure 25: Sectional stress analysis of the tested specimen before cracking phenomenon (State I).

By considering concrete as the reference (γ_1=1), the γ_2 factor can be written as:

$$\gamma_2 = \frac{1}{1 + \frac{\pi^2 A_2 E_2 s}{K L^2}} \quad (9)$$

where K and s are the stiffness and spacing of shear connectors, respectively, and L is the beam span.

The position of the centroid of the composite section, z_c, measured from the upper surface of the concrete slab, can be determined by:

$$z_c = \frac{\sum_{i=1}^{2} (\gamma_i E_i A_i z_i)}{\sum_{i=1}^{2} (\gamma_i E_i A_i)} \quad (10)$$

Once the effective bending stiffness is established, the total normal stresses of the timber and the concrete are computed using the following equations:

$$\sigma_{1,c} = \sigma_1 + \sigma_{m,1,c} = \left[-M \frac{\gamma_1 E_1 a_1}{(EI)_{eff}}\right] + \left[-M \frac{E_1 z_1}{(EI)_{eff}}\right] \quad (11)$$

$$\sigma_{1,t} = \sigma_1 + \sigma_{m,1,t} = \left[-M \frac{\gamma_1 E_1 a_1}{(EI)_{eff}}\right] + \left[M \frac{E_1 (h_1 - z_1)}{(EI)_{eff}}\right] \quad (12)$$

$$\sigma_{2,c} = \sigma_2 + \sigma_{m,2,c} = \left[M \frac{\gamma_2 E_2 a_2}{(EI)_{eff}}\right] + \left[-M \frac{E_2 (h_2 - z_2)}{(EI)_{eff}}\right] \quad (13)$$

$$\sigma_{2,t} = \sigma_2 + \sigma_{m,2,t} = \left[M \frac{\gamma_2 E_2 a_2}{(EI)_{eff}}\right] + \left[M \frac{E_2 z_2}{(EI)_{eff}}\right] \quad (14)$$

where σ_i is the axial stress of the element (i), $\sigma_{m,i,c}$ is the bending stress on the upper surface of the element (i), $\sigma_{i,c}$ is the total normal stress on the upper surface of the element (i), $\sigma_{m,i,t}$ is the bending stress on the lowest

surface of the element (i), $\sigma_{i,t}$ is the total normal stress on the lowest surface of the element (i), M is the bending moment applied on the composite beam, h_1 is the height of the concrete slab, including the concrete drops, and h_2 is the height of the timber cross-section.

It was observed during the experimental tests that the concrete drops were cracked. In order to take into account, the effect of the concrete cracking, the method given in the Eurocode 2 [44] is adopted. This method defines two states: states (I) and (II). For state (I), the whole concrete cross-section is incorporated, whereas only a portion of the concrete cross-section is included in state (II), disregarding the area where the tensile stress exceeds its critical tensile resistance (f_{ctm}).

Before cracking, the concrete is considered to be in state (I). After cracking, the concrete is considered behaving in a mean state between the states (I) and (II). This approach is also adopted by Boccadoro et al. [54].

3.2 State I

In state (I), the entire section of the concrete cross-section is considered uncracked (see Figure 25). The effective flexural stiffness of the composite beam, denoted by $(EI)_{eff,I}$, is computed using Eq. (5) and given in Table 9. It should be noted that K is set to the mean value of K_s at SLS and the mean value of K_u at ULS, both derived from push-out tests (see section 2.1.4). Based on the values provided in the Table 9, it can be first noticed that the degree of composite action is high at both SLS and ULS, as γ_2 in both cases is close to 0.9. It is worth mentioning that the test F_2 exhibited a significantly higher flexural stiffness compared to the tests F_1 and F_3, which had similar flexural stiffness. This is related to the higher strength of concrete, as reported in Table 9. The parameter $z_{c,I}$ is the position of the composite centroid in state (I) and can be computed using Eq. (10).

Table 9: Effective bending stiffness of the composite beams in state (I).

Test	*State*	z_1 [mm]	A_1 [mm²]	E_1 [MPa]	z_2 [mm]	A_2 [mm²]	E_2 [MPa]	s [mm]	K [N/mm]	γ_2	$z_{c,I}$ [mm]	$(EI)_{eff,I}$ [10^{13}Nmm²]
F_1	SLS	60	45844	29050	183	20337	11211	426	177600	0.888	76.3	1.20
	ULS								174680	0.887	76.2	1.20
F_2	SLS	62.4	49468	35179	189.5	20136	11295		177600	0.889	75.6	1.32
	ULS								174680	0.887	75.6	1.32
F_3	SLS	61.5	47632	28340	184.6	19897	11243		177600	0.890	77.3	1.20
	ULS								174680	0.889	77.3	1.20

The bending moment, which causes cracking, can be estimated as follows:

$$M_{cr} = \frac{f_{ctm}(EI)_{eff,I}}{E_1(h_1 - z_{c,I})} \quad (15)$$

According to the Eurocode 2 [44], the critical tensile resistance of concrete (f_{ctm}) can be estimated based on its average compressive resistance (f_{cm}) by:

$$f_{ctm} = 0.3 \times \left(f_{cm}{}^{\frac{2}{3}}\right) \quad (16)$$

Using Eq. (15), the bending moment, M_{cr}, is computed for each flexural test and provided in Table 10.

Table 10: Computation of the cracking bending moment.

Test	f_{cm} [MPa]	f_{ctm} [MPa]	M_{cr} [kN.m]
F_1	25.3	2.6	8.9
F_2	47.8	3.95	12.5
F_3	23.3	2.44	8.6

3.3 State II

In state (II), the concrete section is supposed to undergo cracking, resulting in the formation of the cracked (B) and uncracked zones (A) in the cross-section. z_{ctm} is the level of the transition between the two zones (see Figure 26).

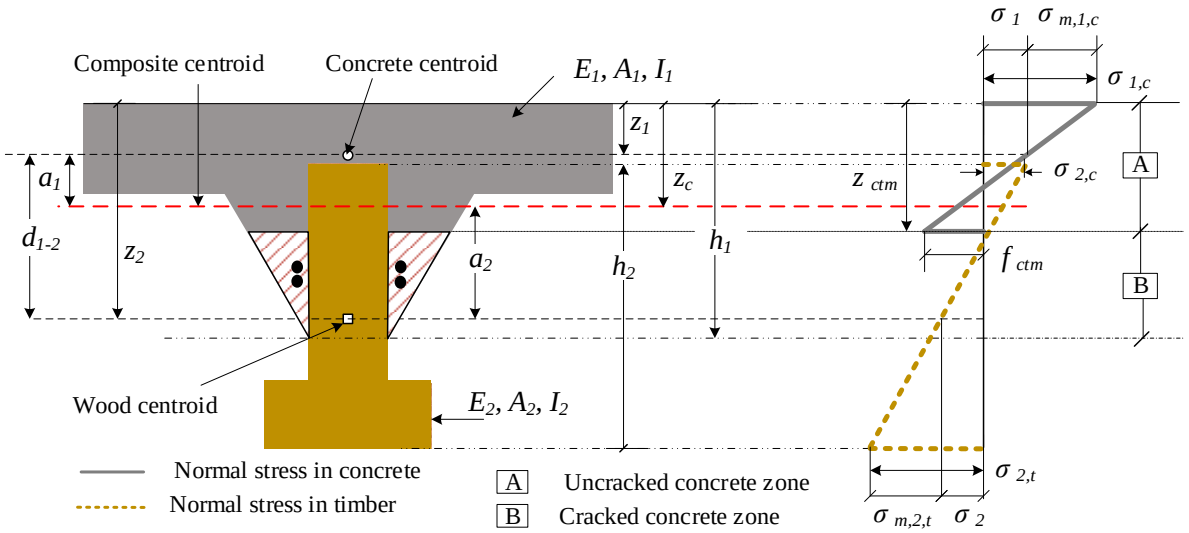

Figure 26: Sectional stress analysis of the tested specimen after cracking phenomenon (State II).

The initial estimation of the parameter z_{ctm}, at a given bending moment M, can be performed as follows:

$$z_{ctm} = \frac{f_{ctm} \times (EI)_{eff,I}}{E_1 M} + z_{c,I} \quad (17)$$

In order to determine the effective bending stiffness of the composite beam in the state (II), the following loop scheme is used:

- **Step 1**: for a given bending moment (M), solve the Eq. (17) to estimate the height of the uncracked concrete fibre (${z_{ctm}}^{j=1}$);
- **Step 2**: define a new uncracked concrete cross section with a height (${h_1}^j$) equal to (${z_{ctm}}^j$);
- **Step 3**: with the new concrete cross-section, update the position of the centroid of the composite cross-section (${z_c}^j$), using Eqs. (6)-(8) and Eq. (10), and compute the new effective flexural stiffness ${(EI)_{eff,II}}^j$ through Eq. (5);
- **Step 4**: compute the total normal stress ($\sigma_{1,t}$) in the lowest concrete fibre, located at (${z_{ctm}}^j$);
- **Step 5**: if the tensile stress ($\sigma_{1,t}$) doesn't exceed the critical resistance of concrete (f_{ctm}), the value of ${z_{ctm}}^j$ corresponds to the position of the uncracked fibre. Otherwise, decrease the parameter ${z_{ctm}}^j$ by Δ,

and repeat the steps from (2) to (5) until the uncracked fibre is found. Subsequently, the flexural stiffness $(EI)_{eff,II}$ of the final composite section is equal to $(EI)_{eff,II}{}^{j}$.

The flowchart of the direct loop scheme to compute the effective flexural stiffness $(EI)_{eff,II}$ is shown in Figure 27. The parameter Δ represents the decrement of the concrete height z_{ctm}, which is set at 1 mm in the present paper.

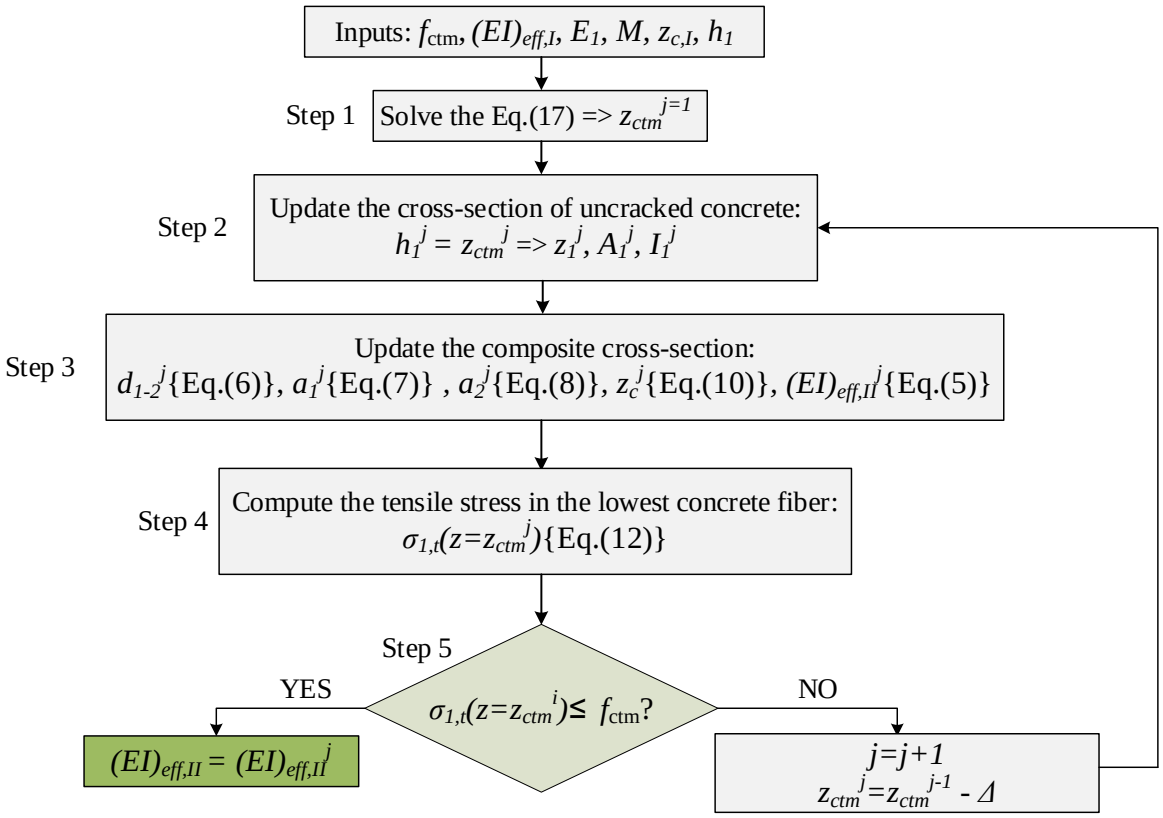

Figure 27: Flowchart of the direct loop scheme for the effective bending stiffness computation.

The effective bending stiffness of the tested specimens in state (II) is denoted as $(EI)_{eff,II,S}$, corresponding to a bending moment M_S of 29.3 kN.m at SLS, whereas it is denoted as $(EI)_{eff,II,U}$, corresponding to a bending moment M_U of 48.3 kN.m, at ULS (see Eq. (21)). Following the flowchart of the direct loop, at both SLS and ULS, the effective bending stiffness of the composite beam is computed and provided in Table 11. It can be noted that at both SLS and ULS, the level z_{ctm} is below the concrete slab in all tests.

Table 11: Effective bending stiffness of the composite beams in state (II).

Test	*State*	h_1 [mm]	z_{ctm} [mm]	$(EI)_{eff,II}$ [10^{13}Nmm^2]
F_1	SLS	206	102	1.0
	ULS		86	0.97
F_2	SLS	213.5	118	1.26
	ULS		94	1.20
F_3	SLS	209.5	101	1.0
	ULS		86	0.97

After determining the flexural stiffness of the specimens at SLS and ULS, the next paragraph will compute the mid-span deflection in state (II) by applying linear interpolation between the two loading levels.

3.4 Analytical force-deflection curve

The combination of the states (I) and (II) can be performed following the instructions provided in Eurocode 2 [44]:

$$w_m = \begin{cases} w_I & \text{for } M \le M_{cr} \\ \zeta w_{II} + (1-\zeta) w_I & \text{for } M > M_{cr} \end{cases} \quad (18)$$

with,

$$w_I = \frac{F}{96(EI)_{eff,I}}[a(3L^2 - 4a^2) + 3(a+b)L^2 - 4(a+b)^3] \quad (19)$$

$$\zeta = 1 - \beta\left(\frac{M_{cr}}{M}\right)^2 \quad (20)$$

$$M = \frac{F}{4}(2a+b) \quad (21)$$

The linear interpolation between SLS and ULS is done as follows:

$$w_{II} = \begin{cases} \frac{F}{96(EI)_{eff,II,S}}[a(3L^2 - 4a^2) + 3(a+b)L^2 - 4(a+b)^3] & \text{for } M_{cr} \le M \le M_{ELS} \\ \frac{F}{96(EI)_{eff,II,U}}[a(3L^2 - 4a^2) + 3(a+b)L^2 - 4(a+b)^3] & \text{for } M > M_{ELS} \end{cases} \quad (22)$$

where w_I and w_{II} are the mid-span deflections of the specimens subjected to 6-point bending test in states (I) and (II), respectively; w is the total mid-span deflection; ζ is a distribution coefficient; β is a coefficient taking account the influence of the loading duration (equal to 1 for a single short-term loading).

The load-deflection curves of the tested specimens before and after concrete cracking are analytically predicted and illustrated in Figure 28, Figure 29, Figure 30, and Annex B.

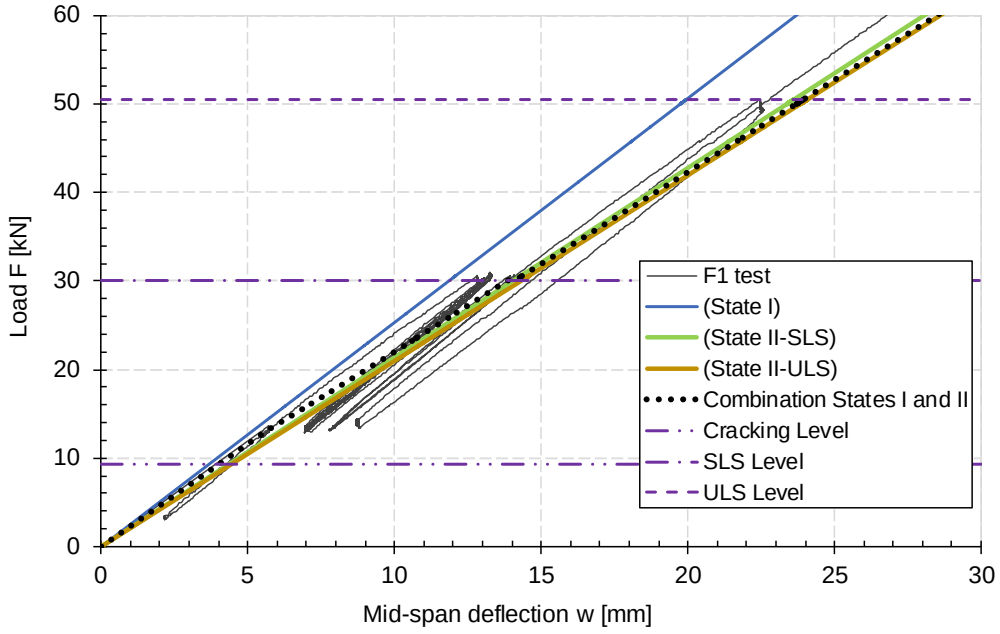

Figure 28: Comparison of predicted and experimental load-deflection curves of the test F_1.

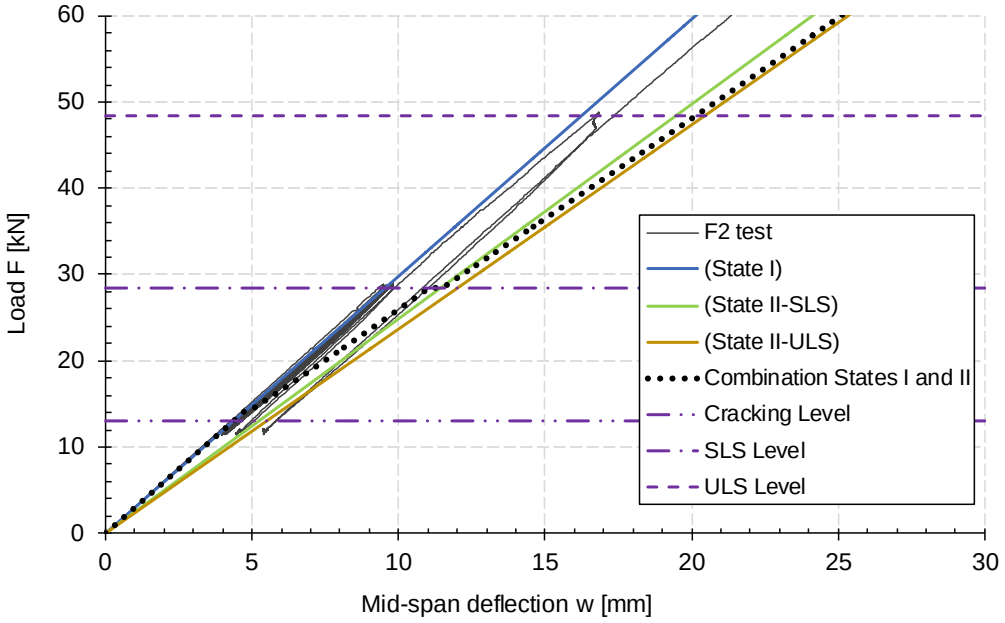

Figure 29: Comparison of predicted and experimental load-deflection curves of the test F_2.

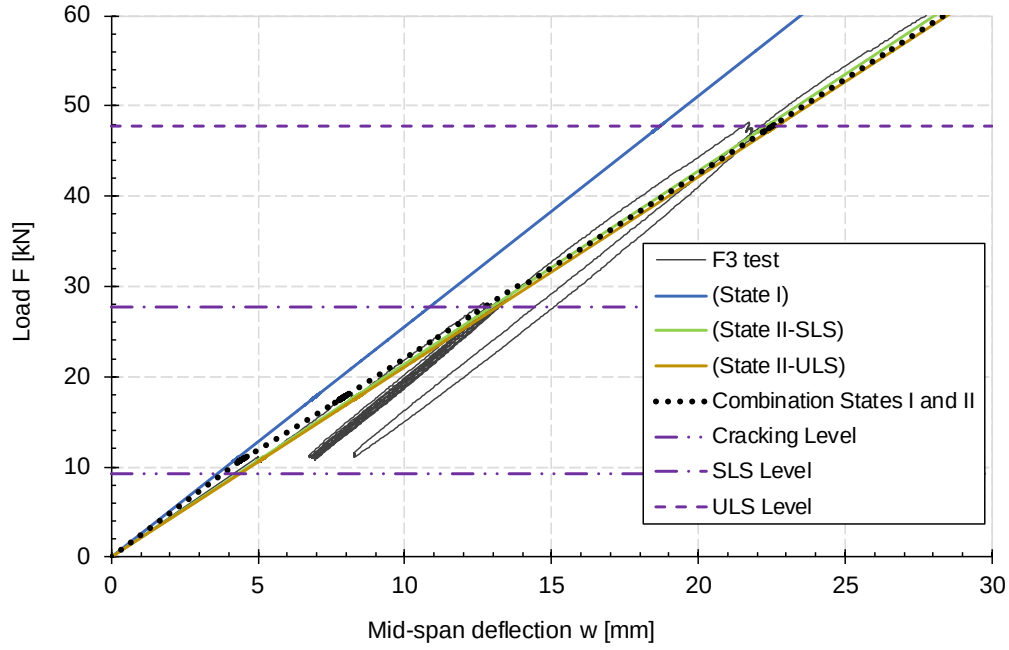

Figure 30: Comparison of predicted and experimental load-deflection curves of the test F_3.

Below the cracking level, the predicted curves match the experimental ones. As the load increases and the critical tensile resistance of concrete is exceeded, the concrete slab exhibits cracking. The predicted behaviour deviates from state (I) and tend to state (II), providing a good fit with the experimental results.

The predicted and experimental mid-span deflections under both SLS and ULS loads are collected in Table 12. The mean errors between the experimental and the predicted mid-span deflections for the three tests at SLS and ULS levels were 8.9% and 9.8%, respectively. In addition, it can be noted that the predicted mid-span deflections w_m and w_{II} were close at both SLS and ULS level, with mean differences of 1.9% and 0.9%, respectively. This

suggests that state (II) appears to be sufficient for estimating the mid-span deflection without the need to combine states (I) and (II) using the Eq. (18). It should also be noted that the errors between the experimental and the predicted mid-span deflections of the tests F_1 and F_3 were smaller than that of test F_2. In fact, the estimation of the deflection by the analytical approach was made by adopting the shear stiffness of the connector obtained from pushout tests. Furthermore, the concrete resistance observed in the push-out test was similar to that of tests F1 and F_3 but lower than that of test F_2. Such a difference in concrete strength might affect the shear performance of the connection, thus explain the discrepancy in test F_2.

Table 12: Comparison of experimental and analytical values of mid-span deflection under SLS and ULS loads.

Test	*Mid-span deflection at SLS*					*Mid-span deflection at ULS*				
	Experimental	Predicted			Error (%)	Experimental	Predicted			Error (%)
		w_I	w_{II}	w_m			w_I	w_{II}	w_m	
F_1	12.24	11.9	14.1	13.8	11.3	21.8	19.9	24.1	24	9.1
F_2	9.47	9.5	11.4	11	13.9	16.7	16.2	20.4	20.1	16.9
F_3	12.7	10.8	12.95	12.9	1.6	21.7	18.7	22.7	22.5	3.5

In order to compare the experimental and the analytical normal stresses, the Eqs. (11)-(14) were used to compute the analytical normal stresses on the upper surface of the concrete slab ($\sigma_{1,c}$) and on the lowest timber fibre ($\sigma_{2,t}$). The values of the calculated normal stresses are reported in Table 13. Based on the results, it can be observed that the analytical γ-method overestimated the normal stress at both SLS and ULS with mean errors of 9.7% and 6.95%, respectively.

Table 13: Comparison of experimental and analytical values of normal stresses under SLS and ULS loads.

Test	Normal stress	*SLS*			*ULS*		
		Experimental	Predicted	Error (%)	Experimental	Predicted	Error (%)
F_1	$\sigma_{1,c}$	4.9	5.3	6.8	8.8	8.7	1.5
	$\sigma_{2,t}$	5.9	6	2.7	9.8	10.2	3.7
F_2	$\sigma_{1,c}$	5	5.6	10.7	8.6	9.2	6.5
	$\sigma_{2,t}$	4.6	5.3	13.2	8	9.3	13.9
F_3	$\sigma_{1,c}$	4.4	5.2	15.4	7.8	8.6	9.3
	$\sigma_{2,t}$	5.5	6.1	9.8	9.5	10.2	6.8

Finally, it can be concluded that the analytical γ-method underestimated the flexural stiffness of the tested specimens and overestimated the normal stresses with a reasonable margin of error, thus leading to a conservative estimation compared to the experimental outcomes.

4. Conclusion and future work

In this paper, a timber-concrete composite (TCC) floor system with three-dimensional (3D) ductile notched connectors is proposed. In this system, the web of the timber beam is embedded into the concrete drops, creating a notched timber-concrete interface with three shear planes. This seeks to improve the shear resistance of the concrete around the notched connectors and to confine the timber within the concrete, promoting ductile behaviour through compression in the timber. The trapezoidal shape of the connection offers geometrical interlocking between the timber and the concrete, eliminating the need for additional mechanical steel elements for uplift resistance.

The behaviour of the 3D notched connection is firstly investigated through three symmetrical push-out tests. The results show that, with the three shear planes provided by the concrete drops, the notched connection offers high shear resistance and stiffness, as compared to usual notched connections with similar dimensions. Moreover, this configuration leads to a failure mode governed by the local compression of timber along the grain direction, providing high ductility with a mean maximum slip of 19.5 mm.

Subsequently, novel inversed 6-point bending tests are conducted on three full-scale timber-concrete floors with a span of 6.55 m in order to investigate the global behaviour of the floors. Due to the non-negligible self-weight of the specimen and the loading device, the test setup is designed to be able to measure deformations, deflections as well as the initial stiffness at a lower load level. Under these bending tests, the TCC floors exhibit a quasi-linear behaviour until a brittle collapse initiated by a tensile rupture of the timber beam. In addition, limited values of the slips and of uplifts were obtained at the maximum force. This demonstrates that an almost full composite action is achieved and that the dovetail shape of the notched connectors is effective in providing a geometrical interlocking between the timber and concrete layers. The results from strain gauges show that the strain distribution of the composite cross-section is almost linear and continuous from the timber to concrete cross-section within SLS and ULS. The curvature of timber and concrete sections can be assumed identical, validating the assumption made in the γ-method. During the bending tests, several loading cycles are also applied to the specimens to assess their impact on the flexural stiffness of the TCC floor. The findings indicate that the degradation of the flexural stiffness caused by contact at the interface between timber and concrete is small but non-negligible. This degradation can be caused by several possible effects, such as creep and local compression of timber around the notched connectors and friction. In this study, it is found that friction effect is negligible. However, this may be due to the painting applied on the timber at the timber-concrete interface, so this conclusion may not be extended to cases without paint.

Lastly, an analytical investigation is performed to determine the flexural stiffness of the TCC floors. In this investigation, the γ-method is adapted to the configuration of the present TCC floor system, while considering the effect of concrete cracking. The outcome demonstrates that the adapted γ-method can be used to estimate the flexural stiffness of the TCC floors, as a conservative estimation of the bending stiffness and stresses is obtained in comparison to the experimental results with acceptable margins of error.

Acknowledgements

The authors gratefully acknowledge financial support by the French National Research Agency (ANR, Paris) and INGENOVA with a grant number ANR-21-CHIN-0003 through the ANR FREEINBTP project.

Annex A.

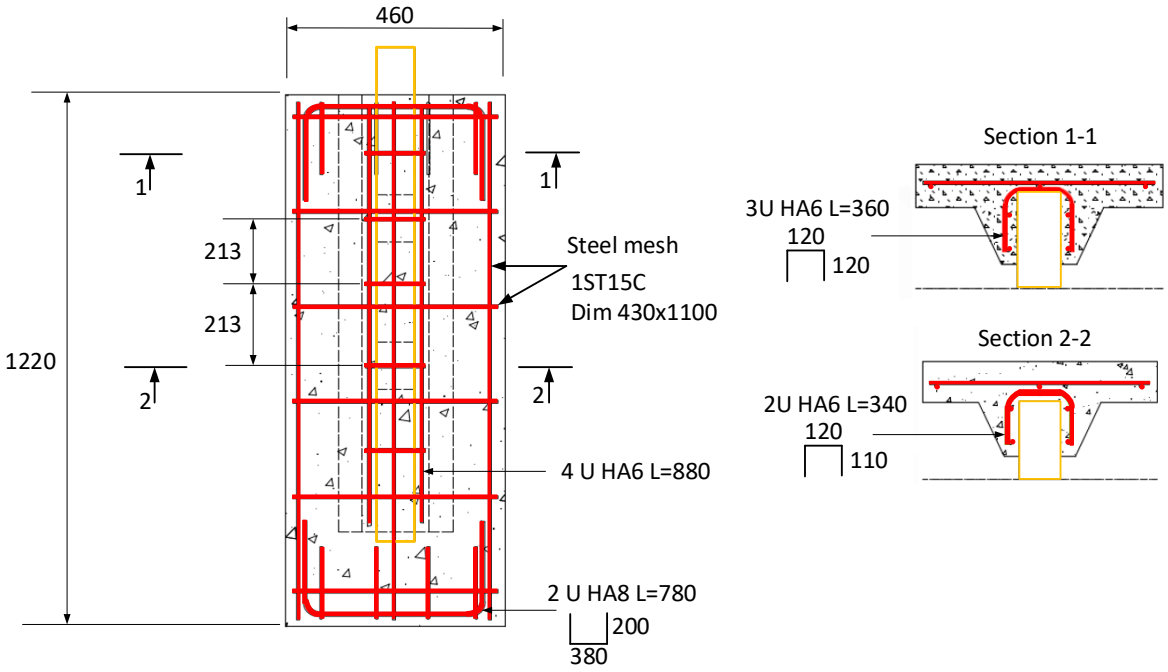

Figure A. 1: Details of the steel rebars used in concrete slab and concrete drops of push-out specimen.

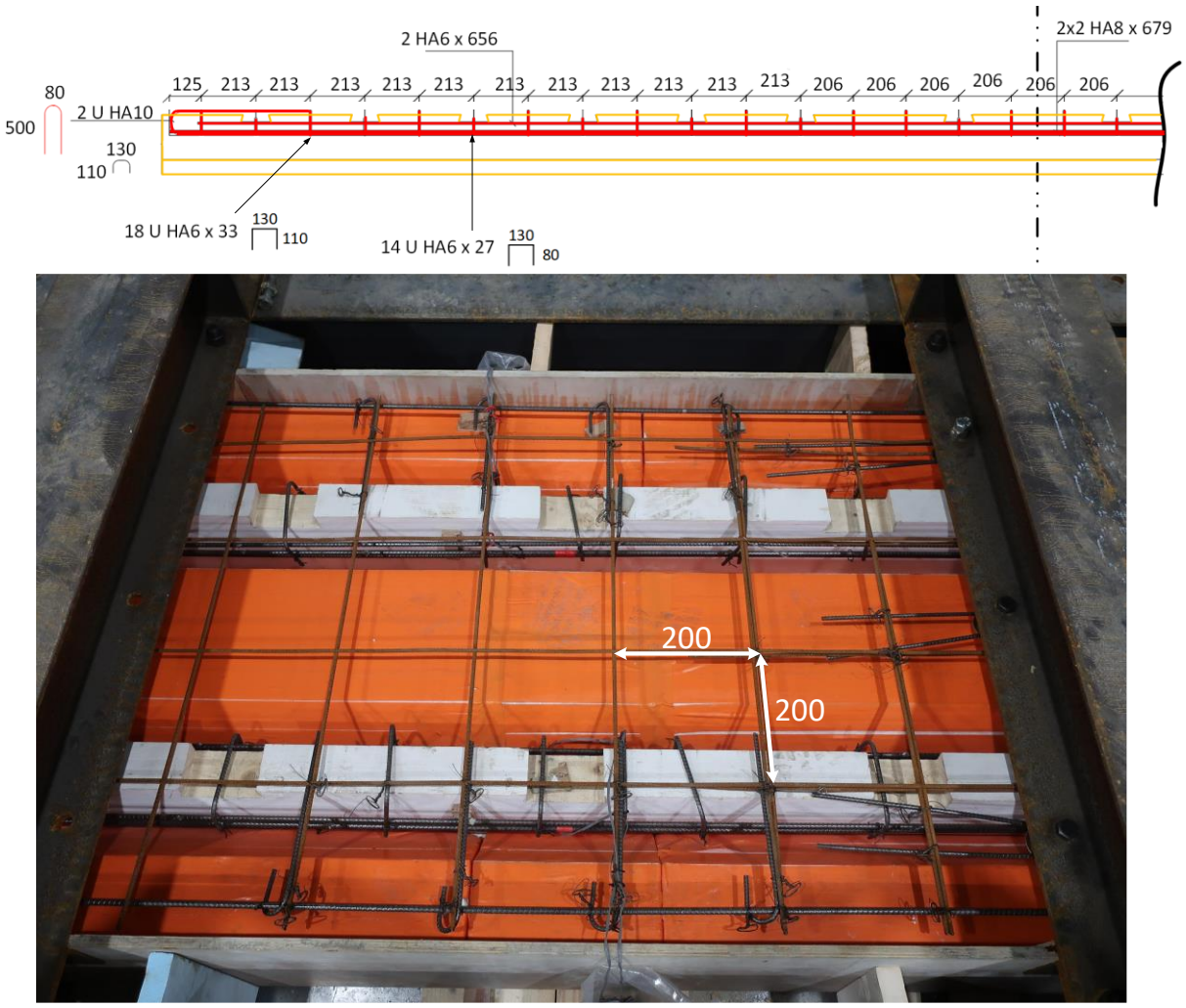

Figure A. 2: Details of the steel rebars cage used in the beam specimen.

Annex B.

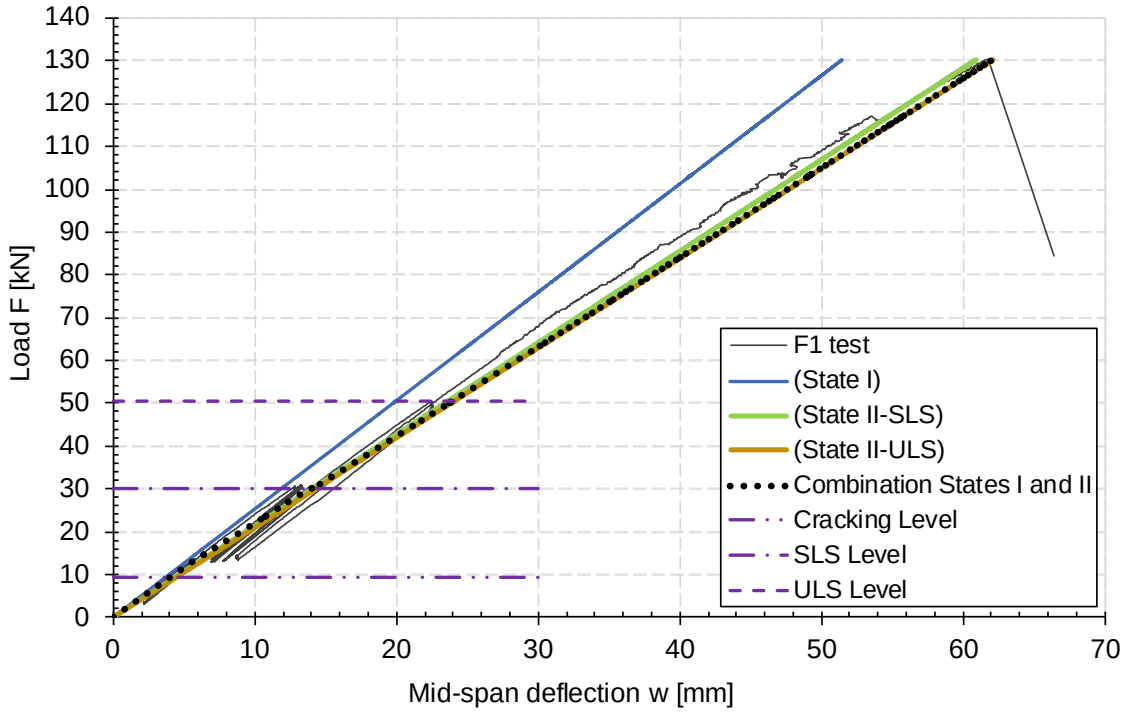

Figure B. 1: Test F_1 – Comparison of predicted and experimental load-deflection curves of the tested specimens up to failure.

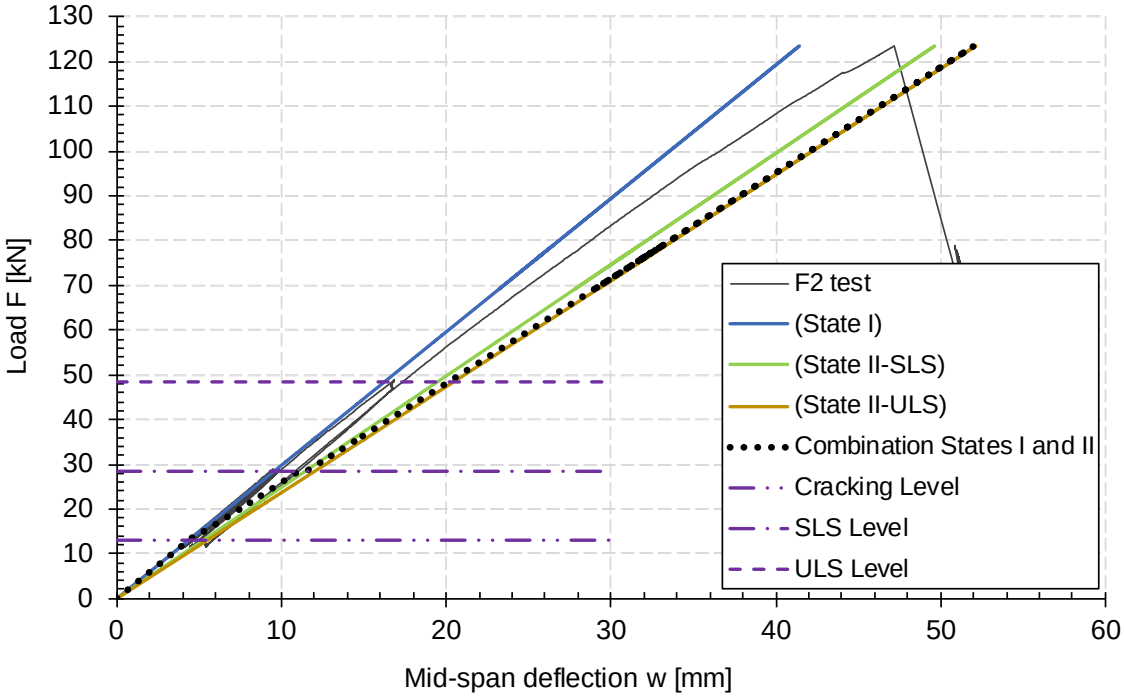

Figure B. 2: Test F_2 – Comparison of predicted and experimental load-deflection curves of the tested specimens up to failure.

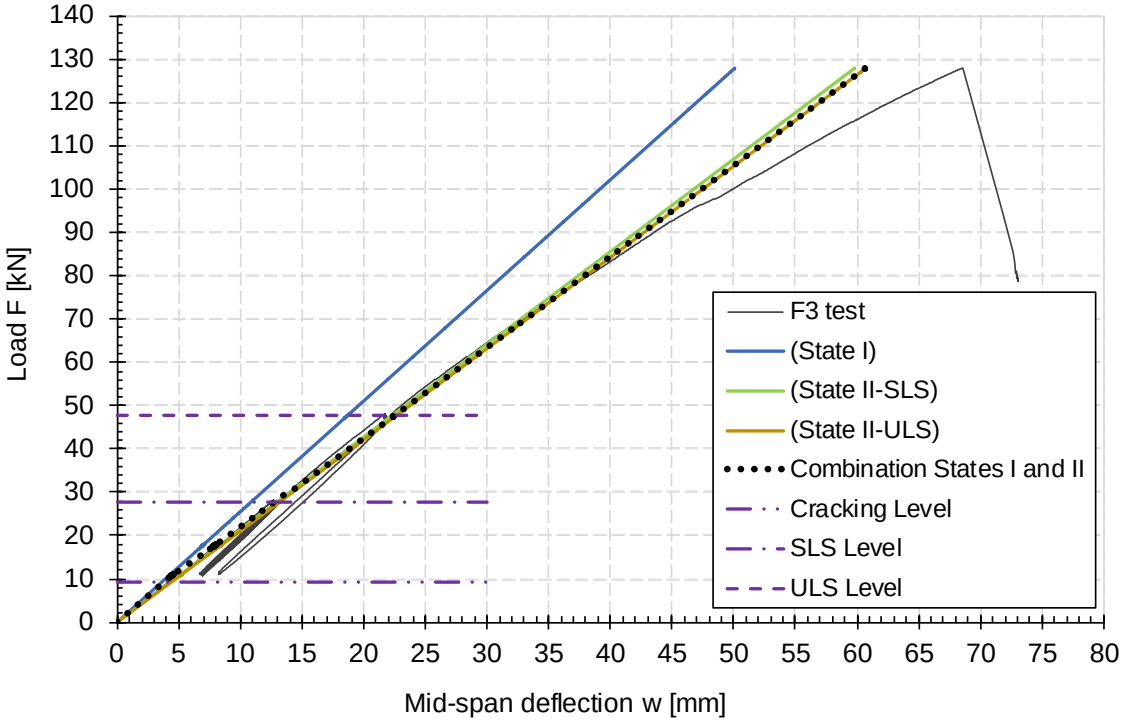

(c) Test F_3

Figure B. 3: Test F_3 – Comparison of predicted and experimental load-deflection curves of the tested specimens up to failure.

References

[1] UNEP, Buildings and Climate Change Summary for Decision- Makers, UNEP DTIE, Sustainable Consumption & Production Branch (2009). www.unep.fr/scp/sun.

[2] M. Zhen, B. Zhang, Energy performance of a light wood-timber structured house in the severely cold region of China, Sustainability 10 (2018) 1501. https://doi.org/10.3390/su10051501.

[3] A. Stocchero, J. K. Seadon, R. Falshaw, M. Edwards, Urban Equilibrium for sustainable cities and the contribution of timber buildings to balance urban carbon emissions: a New Zealand case study, J. Clean. Prod. 143 (2017), pp.1001–1010.

[4] J. Tollefson, the wooden skyscrapers that could help to cool the planet, Nature News 545 (2017) 280.

[5] M. Ramage, H. Burridge, M. Wicher, G. Fereday, T. Reynolds, D. Shah, G. Wu,L. Yu, P. Fleming, D. Densley Tingley, J. Allwood, P. Dupree, P.F. Linden,O. Scherman, The wood from the trees: the use of timber in construction, Renew Sustain. Energy Rev. 68 (2017), pp.333–359. https://doi.org/10.1016/j.rser.2016.09.107.

[6] B. L. Deam, M. Fragiacomo, A. H. Buchanan, Connections for composite concrete slab and LVL flooring systems. Mater Struct 41 (2008), pp.495–507.

[7] A. Ceccotti, Composite concrete-timber structures, Progress Struct. Eng. Mater. 4 (3) (2002) pp.264 275.

[8] X. Zhang, X. Hu, H. Gong, J. Zhang, Z. Lv, W. Hong, Experimental study on the impact sound insulation of cross laminated timber and timber-concrete composite floors, Appl. Acoust. 161 (2020), 107173.

[9] C. Martins, P. Santos, P. Almeida, A. Dias, Acoustic performance of timber and timber-concrete floors. Constr Build Mater (2015), pp.684–691. https://doi.org/10.1016/j.conbuildmat.2015.10.142.

[10] Z. Xie, X. Hu, H. Du, X. Zhang, Vibration behavior of timber-concrete composite floors under human-induced excitation, Journal of Building Engineering 32 (2020), 101744.

[11] A. Frangi, M. Fontana, E. Hugi, R. Jöbstl, Experimental analysis of cross-laminated timber panels in fire. Fire Safety J 44(8) (2009). https://doi.org/10.1016/j. firesaf.2009.07.007.

[12] F. E. Richart, and C. B. Williams, Tests of composite timber concrete beams. Proc., American Concrete Institute (1943) 39, pp.253–262.

[13] W.M. Sebastian, M. Piazza, T. Harvey, T. Webster, Forward and Reverse shear transfer in beech LVL-concrete composites with singly inclined coach screw connectors. Eng Struct 175 (2018), pp.231–244. https://doi.org/10.1016/j.engstruct.2018.06.070.

[14] E. Steinberg, R. Selle, T. Faust, Connectors for Timber– Lightweight Concrete Composite Structures. J Struct Eng 129 (2003), pp.1538–1545.

[15] A.M.P.G. Dias, S.M. Lopes, J-W. van de Kuilen, H.M.P. Cruz, Load-carrying capacity of timber-concrete joints with dowel-type fasteners. J Struct Eng 133 (2007). http://dx.doi.org/10.1061/(asce)0733-9445(2007)133:5(720).

[16] A.M.P.G. Dias, S.M. Lopes, J-W. van de Kuilen, H.M.P. Cruz, Stiffness of dowel-type fasteners in timber–concrete joints. Proc Inst Civ Eng Struct Build 163 (2010). https://doi.org/10.1680/stbu.2010.163.4.257.

[17] P. Pincus, Behaviour of wood concrete composite beams. J. Struct. Div. 96 (1970), pp.2009–2019.

[18] T. Godycki, J. Pawlica, and J. Kleszczewski, Concrete decks with wooden joists/Verbunddecke aus Holzrippen und Betonplatte. Bauingenieur, 59 (1984), pp. 477-483.

[19] A. Ceccotti, Composite concrete-timber structures. Prog. Struct. Eng. Mater. 4 (2022), pp.264–275.

[20] U. Kuhlmann, B. Michelfelder, Grooves as Shear-Connectors in Timber-Concrete Composite Structures. Proceedings of the 8th World Conference on Timber Engineering, Lahti, Finland (2004).

[21] D. Yeoh, M. Fragiacomo, M.D. Franceschi, A.H. Buchanan, Experimental Tests of Notched and Plate Connectors for LVL-Concrete Composite Beams. J Struct Eng ASCE 137 (2011). https://doi.org/10.1061/(ASCE)ST.1943-541X.0000288.

[22] M. Brunner, M. Romer, M. Schnüriger, Timber-concrete-composite with an adhesive connector (wet on wet process). Mat Struct 40 (2007).

[23] J.H.J.D.O. Negrão, C.A.L.D. Oliveira, F.M.M.D. Oliveira, PB. Cachim, Glued composite timber-concrete beams. I: Interlayer connection specimen tests. J Struct Eng ASCE 136 (2010). https://doi.org/10.1061/(ASCE)ST.1943-541X.0000228.

[24] L.A. Bathon, and P. Clouston, Experimental and numerical results on semi pre-stressed wood-concrete composite floor systems for long span applications. In Proc., 8th World Conf. on Timber Engineering (2004), pp.339–344. Lathi, Finland: Finnish Association of Civil Engineers, RIL.

[25] J.H. Negrão, F.M. Oliveira, C.L. Oliveira, Investigation on timber-concrete glued composites. In *9th World Conference on Timber Engineering (WCTE 2006). Portland, Oregon, USA*.

[26] G. Ferrara, L. Michel, E. Ferrier, Flexural behaviour of timber-concrete composite floor systems linearly supported at two edge. Journal of Engineering Structures 281 (2023). https://doi.org/10.1016/j.engstruct.2023.115782.

[27] J. Frohnmüller, J. Fischer, W. Seim, Full-scale testing of adhesively bonded timber-concrete composite beams. Mater Struct 54 (2021), pp.1–21. https://doi.org/10.1617/s11527-021-01766-y.

[28] L. Xie, G. He, X. Wang, P.J. Gustafsson, R. Crocetti, L. Chen, et al, Shear capacity of stud-groove connector in glulam-concrete composite structure. BioResources 12 (2017), pp.4690–4706.

[29] D. Yeoh, M. Fragiacomo, P. Aldi, M. Mazzilli, U. Kuhlmann, Performance of notched coach screw connection for timber-concrete composite floor system. Proceedings 10th world conference on timber engineering, Miyazaki, Japan. 2008. p. 221.

[30] P. K. Rasmussen, J. H. Sørensen, L. C. Hoang, B. Feddersen, F. Larsen, Notched connection in timber-concrete composite deck structures, A literature review on push-off experiments & design approaches. Construction and Building Materials 397 (2023). https://doi.org/10.1016/j.conbuildmat.2023.131761.

[31] B.L. Deam, M. Fragiacomo, and A. H. Buchanan, Connections for composite concrete slab and LVL flooring systems. Mater. Struct. 41 (2008), pp.495–507. https://doi.org/10.1617/s11527-007-9261-x.

[32] V. Ouch, P. Heng, Q.-H. Nguyen, H. Somja, and Thierry Soquet, An experimental investigation on the dovetail notched connection for cross-laminated-timber-concrete composite slabs. European Journal of Environmental and Civil Engineering (2023). DOI: 10.1080/19648189.2023.2194351

[33] D.D. Djoubissie, A. Messan, E. Fournely, A. Bouchaïr, Experimental study of the mechanical behavior of timber-concrete shear connections with threaded reinforcing bars. Engineering Structures 172 (2018), pp. 997-1010. https://doi.org/10.1016/j.engstruct.2018.06.084.

[34] AFNOR, NF EN 338: Structural timber-Strength classes, 2016.

[35] Eurocode 5, Design of Timber Structures. Part 1-1: General - Common Rules and Rules for Buildings. EN 1995-1-1, Brussels, 2004.

[36] AFNOR, NF EN 408: Structural timber and glued laminated timber, 2012.

[37] AFNOR, NF EN 12390-3: Testing hardened concrete – Part 3: compressive strength of test specimens, 2019.

[38] European standard EN 26891, Timber Structures - Connections Made With Mechanical Fasteners General Principles for the Determination of Strength and Deformation Characteristics, CEN, Brussels (1991).

[39] La recherche agronomique pour le développement, cirad, les principales caractéristiques technologiques de 245 essences forestières tropicales, France, 2012. https://tropix.cirad.fr/technical-sheets-available.

[40] Bureau de normalisation (BNETC), XP CEN/TS 19103 Conception et calcul des structures - Calcul des structures mixtes bois-béton - Règles communes et règles pour les bâtiments, BNTEC, 2022.

[41] Y. Jiang, X. Hu, W. Hong, J. Zhang, Experimental Study on Notched Connectors for Glulam-lightweight Concrete Composite Beams. BioResources 15(2) (2020), pp.2171-2180. http://dx.doi.org/10.15376/biores.15.2.2171-2180.

[42] D. Yeoh, M. Fragiacomo, M. De Franceschi, A. H. Buchanan, Experimental Tests of Notched and Plate Connectors for LVL-Concrete Composite Beams. Journal of Structural Engineering 137 (2011), pp. 261-269. https://doi.org/10.1061/(ASCE)ST.1943-541X.0000288.

[43] S.J. Pang, K.S. Ahn, S.m. Jeong, G.C. Lee, H.S. Kim, J.K. Oh, Prediction of bending performance for a separable CLT-concrete composite slab connected by notch connectors. Journal of Building Engineering 49 (2022). https://doi.org/10.1016/j.jobe.2021.103900.

[44] European standard NF EN 1992-1-1, Eurocode 2: Design of concrete structures – Part 1-1: General rules and rules for building, 2005.

[45] Metallic materials – Tensile testing - Part 1: Method of test at room temperature (ISO 6892-1:2019).

[46] E. Martín-Gutiérrez, J. Estévez-Cimadevila, F. Suárez-Riestra, D. Otero-Chans, Flexural behaviour of a new timber-concrete composite structural flooring system. Full scale testing. Building Engineering 64 (2023). https://doi.org/10.1016/j.jobe.2022.105606.

[47] COST Action FP1402. Design of Timber-Concrete Composite Structures: A State-of-the-Art Report by COST Action FP1402/WG 4, 1st ed.; Dias, A., Schänzlin, J., Dietsch, P., Eds.; Shaker Verlag: Aachen, Germany (2018). ISBN 9783844061451.

[48] L. Zhang, J. Zhou, Y.H. Chui, Development of high-performance timber-concrete composite floors with reinforced notched connections. Structures 39 (2022), pp.945-957. https://www.sciencedirect.com/science/article/pii/S2352012422002429.

[49] Y. Zhang, G.M. Raftery, P. Quenneville, Experimental and Analytical Investigations of a Timber–Concrete Composite Beam Using a Hardwood Interface Layer. Journal of Structural Engineering 145 (2019). https://doi.org/10.1061/(ASCE)ST.1943-541X.0002336.

[50] B. Kreis, W. Kübler, A. Frangi, Development and investigation of an innovative, lightweight, two-way spanning timber-concrete composite slab. Engineering Structures 286 (2023). https://doi.org/10.1016/j.engstruct.2023.116087.

[51] S.T. Deresa, J. Xu, B. Shan, H. Ren, Y. Xiao, Experimental investigation on flexural behaviour of full-scale glued laminated bamboo (glubam)-concrete composite beams: A case study of using recycled concrete aggregates. Engineering Structures 233 (2021). https://doi.org/10.1016/j.engstruct.2021.111896.

[52] M.W. Hammad, H.R. Valipour, T. Ghanbari-Ghazijahani, M.A. Bradford, Timber-timber composite (TTC) beams subjected to hogging moment. Construction and Building Materials 321 (2022). https://doi.org/10.1016/j.conbuildmat.2021.126295.

[53] L. Boccadoro, S. Zweidler, R. Steiger, A. Frangi, Bending tests on timber-concrete composite members made of beech laminated veneer lumber with notched connection. Engineering Structures 132 (2017), pp.14-28. https://doi.org/10.1016/j.engstruct.2016.11.029.

[54] L. Boccadoro, Timber-concrete composite slabs made of beech laminated veneer lumber with notched connection, ETH Zürich (2016), https://doi.org/10.3929/ethz-a-010777925.

[55] S.A. Hadigheh, R. McDougall, C. Wiseman, L. Reid, Evaluation of composite action in cross laminated timber-concrete composite beams with CFRP reinforcing bar and plate connectors using Digital Image Correlation (DIC). Engineering Structures 232 (2021). https://doi.org/10.1016/j.engstruct.2020.111791.

[56] European standard EN 1994-1-1, Eurocode 4: Design of composite steel and concrete structures - Part 1-1: General rules and rules for buildings, CEN, Brussels (2004).

[57] European standard NF EN 1991-1-1, Eurocode 1: Actions on structures – Part 1-1: General actions - Densities, self-weight, imposed loads for buildings, (2003).

[58] European standard NF EN 1990-1-1, Eurocode 0: Basis of structural design, CEN, Brussels (2004).

[59] https://www.france-poutres.com/